

# Extrusion-Based 3D Printing of Hierarchically Porous Advanced Battery Electrodes

Steven D. Lacey, Dylan J. Kirsch, Yiju Li, Joseph T. Morgenstern, Brady C. Zarket, Yonggang Yao, Jiaqi Dai, Laurence Q. Garcia, Boyang Liu, Tingting Gao, Shaomao Xu, Srinivasa R. Raghavan, John W. Connell, Yi Lin,\* and Liangbing Hu\*

A highly porous 2D nanomaterial, holey graphene oxide (hGO), is synthesized directly from holey graphene powder and employed to create an aqueous 3D printable ink without the use of additives or binders. Stable dispersions of hydrophilic hGO sheets in water ( $\approx 100 \text{ mg mL}^{-1}$ ) can be readily achieved. The shear-thinning behavior of the aqueous hGO ink enables extrusion-based printing of fine filaments into complex 3D architectures, such as stacked mesh structures, on arbitrary substrates. The freestanding 3D printed hGO meshes exhibit trimodal porosity: nanoscale (4–25 nm through-holes on hGO sheets), microscale (tens of micrometer-sized pores introduced by lyophilization), and macroscale ( $< 500 \mu\text{m}$  square pores of the mesh design), which are advantageous for high-performance energy storage devices that rely on interfacial reactions to promote full active-site utilization. To elucidate the benefit of (nano) porosity and structurally conscious designs, the additive-free architectures are demonstrated as the first 3D printed lithium–oxygen ( $\text{Li-O}_2$ ) cathodes and characterized alongside 3D printed GO-based materials without nanoporosity as well as nanoporous 2D vacuum filtrated films. The results indicate the synergistic effect between 2D nanomaterials, hierarchical porosity, and overall structural design, as well as the promise of a freeform generation of high-energy-density battery systems.

Additive manufacturing (AM) techniques, such as 3D printing, have garnered much attention in the scalable development of functional components and structures for a range of applications including energy,<sup>[1,2]</sup> electronics,<sup>[3]</sup> biomedicine<sup>[4,5]</sup> as well as high-performance composites for automotive and aircraft manufacturing.<sup>[6]</sup> Extrusion-based 3D printing is an inexpensive and simple fabrication method that relies on highly concentrated supporting media and a three-axis motion stage to create complex structural forms layer-by-layer.<sup>[7]</sup> Among the numerous supporting media materials, graphene oxide (GO) has been shown to possess unique rheological properties when dispersed in high concentrations in a green solvent such as water ( $\text{H}_2\text{O}$ ), which is advantageous for scalable and eco-friendly 3D printing methods.<sup>[2,8–11]</sup> However, the predominant applications of 3D printed GO have been mainly limited to supercapacitors<sup>[12–16]</sup> and lithium-ion batteries.<sup>[2,17,18]</sup> To the best of our knowledge, 3D printable GO inks have not been applied to higher-energy-density battery technologies, especially lithium–oxygen ( $\text{Li-O}_2$ ) batteries.

Herein, extrusion-based printing was employed to successfully create complex hierarchical porous structures, which were demonstrated as the first 3D printed  $\text{Li-O}_2$  cathodes. An additive-free and aqueous carbon-based ink was produced by oxidizing holey graphene (hG), a highly porous carbon nanomaterial, to create a nanoporous, hydrophilic GO material known as holey graphene oxide (hGO). By adding hGO to a green solvent (i.e.,  $\text{H}_2\text{O}$ ) at high concentrations ( $\approx 100 \text{ mg mL}^{-1}$ ), a printable hGO ink with shear-thinning behavior can be produced and extruded into complex 3D architectures such as stacked mesh structures. The 3D printed hGO mesh possesses multiple levels of porosity (macroscale  $\rightarrow$  nanoscale), which enables pathways for electrolyte and oxygen gas to enhance  $\text{Li-O}_2$  battery performance. The results demonstrate the promise of 3D printing toward the fabrication and improvement of advanced energy storage devices as well as the importance of hierarchical porous electrode designs.

Due to a facile one-step oxidation treatment, commercial graphene powder can be transformed into a highly porous

S. D. Lacey, D. J. Kirsch, Y. Li, J. T. Morgenstern, Y. Yao, J. Dai, B. Liu, T. Gao, Dr. S. Xu, Prof. L. Hu  
Department of Materials Science and Engineering  
University of Maryland  
College Park, MD 20742-4111, USA  
E-mail: binghu@umd.edu

Dr. B. C. Zarket, Prof. S. R. Raghavan  
Department of Chemical and Biomolecular Engineering  
University of Maryland  
College Park, MD 20742-4111, USA

L. Q. Garcia, Dr. J. W. Connell  
Advanced Materials and Processing Branch  
NASA Langley Research Center  
Mail Stop 226, Hampton, VA 23681-2199, USA

Dr. Y. Lin  
National Institute of Aerospace  
100 Exploration Way, Hampton, VA 23666-6147, USA  
E-mail: yi.lin-1@nasa.gov

 The ORCID identification number(s) for the author(s) of this article can be found under <https://doi.org/10.1002/adma.201705651>.

DOI: 10.1002/adma.201705651

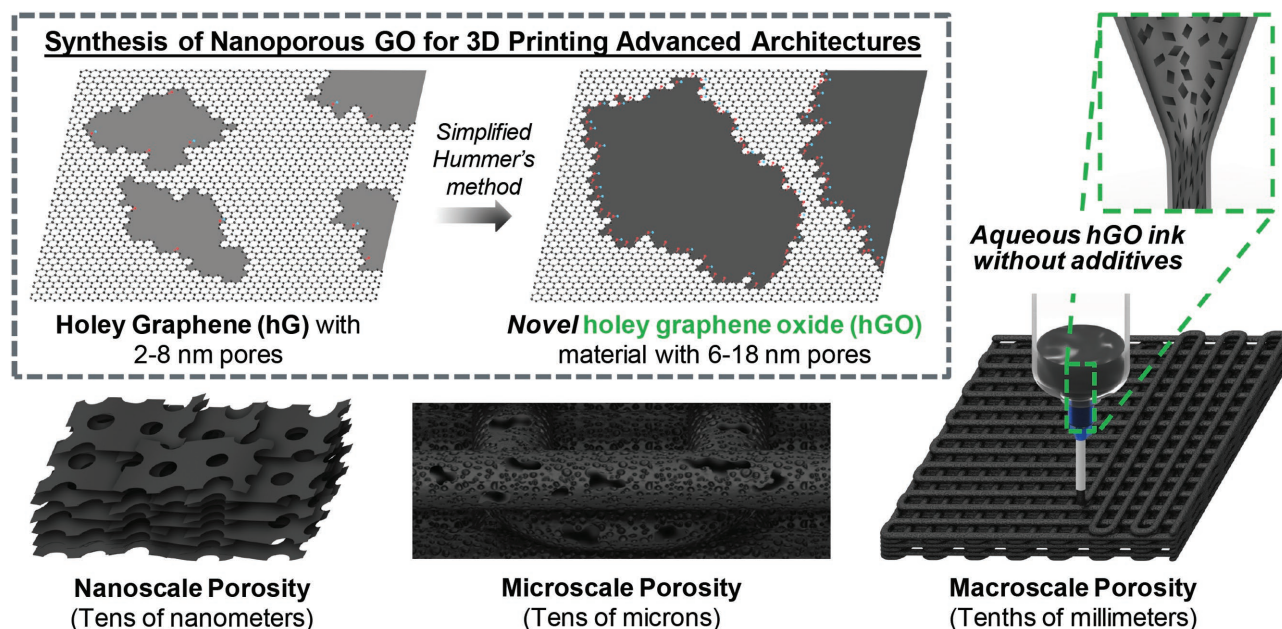


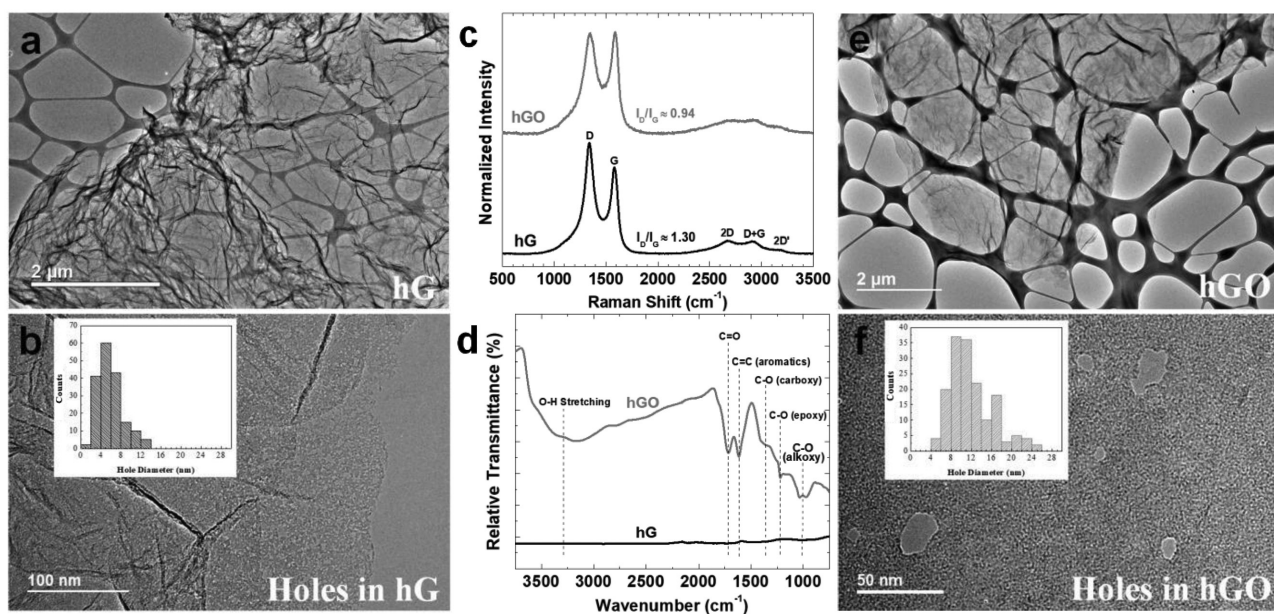
**Figure 1.** Schematic representation of the processes used to synthesize hGO, a highly porous 2D nanomaterial, as well as create an aqueous and additive-free 3D printable hGO ink for extruding complex 3D architectures with hierarchical porosity (macroscale → nanoscale).

nanomaterial, referred to as hG, where both the hole size and density can be carefully controlled by the synthesis conditions.<sup>[19,20]</sup> During hG synthesis, nanosized through-holes are formed by removing defective carbons on the pristine graphene sheets. Our previous works have shown that the porous nature of the as-prepared hG from a single-step controlled air oxidation process has been advantageous for a range of energy storage devices including lithium-ion batteries,<sup>[21]</sup> Li–O<sub>2</sub>, and Li–CO<sub>2</sub> batteries<sup>[22–25]</sup> as well as supercapacitors<sup>[19,26]</sup> due to improved accessible surface area and less tortuous ion-conduction pathways. Alternatively processed hG<sup>[27–30]</sup> and hG composites<sup>[31]</sup> have also been employed in similar electrochemical systems with impressive performance due to rapid charge transport and overall enhancements in diffusion kinetics. In this study, hG was selected as the carbon precursor to produce a highly porous GO material, referred to as hGO, that can be made into an aqueous and additive-free ink for extrusion-based 3D printing. The scheme shown in **Figure 1** displays the hGO synthesis process and ink formulation to create hierarchically porous mesh architectures via AM. The extrusion printed mesh architectures offer trimodal porosity (macroscale, microscale, and nanoscale) due to the inherently nanoporous hGO material (tens of nanometer-sized through-holes) as well as the macroscale 3D mesh design (tenths of millimeter square pores) with lyophilization-induced microscale pores (tens of micrometers).

The size of the synthesized porous 2D nanomaterials (hG and hGO) can be elucidated by transmission electron microscopy (TEM). **Figure 2a,b** and **Figure S1** (Supporting Information) display the sheet structure and hole sizes of the starting hG material via TEM. The hG sheets are extremely thin ( $\approx 5\text{--}7$  layers or  $\approx 2$  nm average thickness) with large lateral dimensions exceeding several micrometers (**Figure 2a**). **Figure 2b** exhibits an array of nanosized through-holes that encompass the entire

hG flake surface. Statistical analyses on numerous hG flake locations indicated an average hole diameter of 5.9 nm with a predominant range between 2 and 8 nm (inset in **Figure 2b**). Due to the nanosized holes, hG is a highly compressible carbon material that can be molded into nearly any shape as demonstrated by our previous works.<sup>[22,23,32]</sup> The graphitic degree of the as-prepared hG can be divulged by Raman spectroscopy (**Figure 2c**). Similar to conventional graphene, hG exhibits D and G bands centered at  $\approx 1342$  and  $\approx 1580$  cm<sup>-1</sup>, respectively. The intensity ratio between the D and G bands (i.e.,  $I_D/I_G$  or  $sp^3/sp^2$  ratio) for hG is  $\approx 1.30$ , which is slightly smaller than the starting intact graphene due to the selective removal of some defective carbon via air oxidation.<sup>[20]</sup> Fourier transform infrared spectroscopy (FTIR) was used to identify the extent of oxygen functional groups on the hG sheets. **Figure 2d** shows that hG has some oxygen-containing functional groups that decorate the sheets and hole perimeters, as confirmed previously.<sup>[19,20]</sup> However, the amount of functional groups introduced by the air oxidation preparation procedure is not sufficient to introduce hydrophilic behavior. Therefore, to create an aqueous 3D printable ink with hG, additional chemical processes or the use of additives would be required to adjust the nanomaterial's surface energy and enable hydrophilicity.

A facile method to induce hydrophilicity in graphene is to use the well-known modified Hummer's method to create GO.<sup>[33]</sup> Typically, bulk graphite is broken down into thinner graphene sheets by mechanical methods and undergoes oxidation by chemical means to create GO. Herein, we altered the modified Hummer's method, deemed the simplified Hummer's method, to produce hGO directly from hG instead of its bulk counterpart. Due to the synthesis conditions of the "simplified Hummer's method," the lateral size of the hGO flakes is preserved however, the hole diameters substantially increase in size due to the oxidation of defective sites (**Figure 2e,f**;



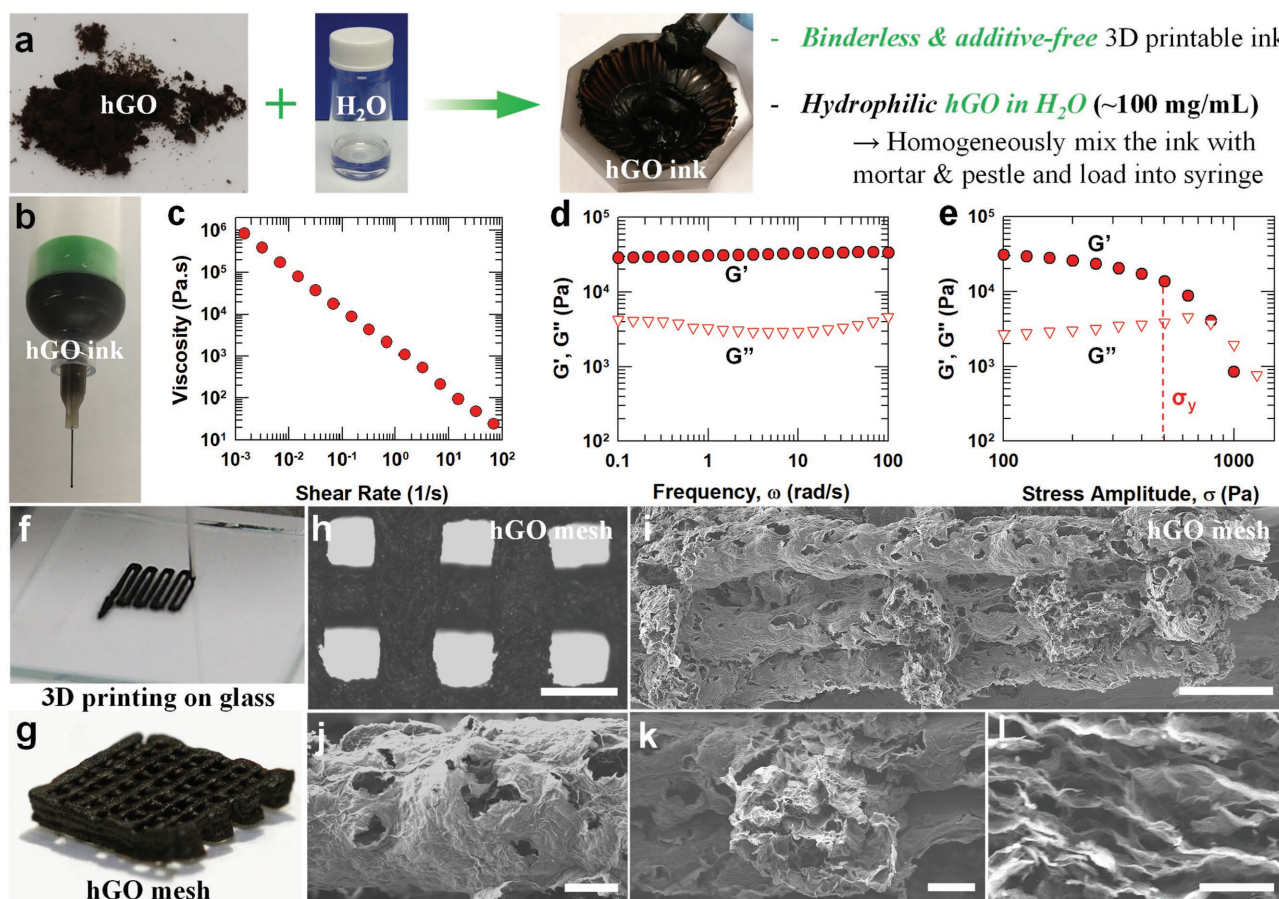
**Figure 2.** Characterization of highly porous 2D nanomaterials: hG and hGO. TEM images showing: a) hG flakes with micrometer lateral dimensions, as well as predominantly b) 2–8 nm holes through the sheet thickness. Inset in (b) shows the hole size distribution for hG. c) Raman spectra of the holey carbon-based materials, where the  $I_D/I_G$  ratio indicates that hGO is less disordered than hG. d) FTIR of both 2D nanomaterials. Numerous oxygen-containing functional groups are present in the synthesized hGO material, which verifies oxidation induced by the simplified Hummer's method as well as the material's hydrophilicity. e,f) Microscopy images of micrometer-sized hGO sheets with 4–25 nm through-holes. The hole size distribution for hGO is wider than hG, as shown by the inset in (f).

Figure S2, Supporting Information). Note that it is expected that the defective hGO flake edges also diminish on the order of nanometers, which is simply insignificant compared to the few micrometer lateral sheet dimensions. The inset in Figure 2f displays a wider distribution of through-hole diameters for hGO (4 to 25 nm) compared to hG (2 to 14 nm). Specifically, the predominant hole sizes for hGO range between 6 and 18 nm with a mean hole diameter of 12.5 nm. Raman spectroscopy shows that the as-prepared hGO is less disordered ( $I_D/I_G \approx 0.94$ ) than the starting hG material. This lower  $I_D/I_G$  ratio likely stems from the removal of more defective carbon during the oxidation process of hG into hGO, which results in the remaining carbon appearing more “ordered” or “crystalline” despite the increase in hole diameters. Note that a similar trend was reported by our group, where hG samples exhibited lower  $I_D/I_G$  ratios compared to the non-hole starting graphene.<sup>[20]</sup> The FTIR results demonstrate that the synthesis conditions induce complete oxidation due to the extent of oxygen-containing functional groups (carboxy, epoxy, alkoxy, aromatics, among others) present on the hGO sheets/hole perimeters. Therefore, unlike the starting hG material, the highly porous hGO material is hydrophilic.

The hydrophilic behavior of hGO enables stable dispersions in  $H_2O$ . To create a 3D printable ink, the rheological properties of the material need to be tuned. Suitable inks must possess high viscosity and paste or gel-like character at rest, but must exhibit shear-thinning behavior to enable the ink to be extruded through fine nozzles. Previous reports have shown that highly concentrated GO dispersions in  $H_2O$  exhibit the appropriate rheology to print fine features and enable complex 3D architectures.<sup>[2,8,18]</sup> Functionalization of GO in suspensions

with responsive polymers and other additives (binders, viscosifiers, among others) has also been advantageous in terms of controlling and improving both ink composition and viscoelasticity.<sup>[34,35]</sup> Figure 3a depicts the process to create an additive-free 3D printable ink from the as-prepared hGO powder and a few mL of  $H_2O$ . By mixing hGO and  $H_2O$  at high concentrations ( $\approx 100 \text{ mg mL}^{-1}$ ), a suitable ink is developed for extrusion printing, as shown in Figure 3b.

Rheological tests were conducted at ambient temperature to elucidate the properties of the aqueous and additive-free hGO ink (Figure 3c–e). Figure 3c shows the apparent viscosity as a function of shear rate. At low shear-rates, the viscosity approaches infinity, indicating that the ink acts as a solid at low shear or at rest (i.e., the material is a Bingham plastic with a yield stress). This is further borne out by the oscillatory frequency sweep results shown in Figure 3d. Here, the elastic/storage modulus  $G'$  and the viscous/loss modulus  $G''$  are plotted as functions of the angular frequency. Both moduli are independent of frequency and  $G'$  is approximately an order-of-magnitude higher than  $G''$ , indicating that the sample behaves like an elastic solid. The frequency-independence of the moduli means that the sample does not relax at long time-scales, which suggests that the hGO sheets that compose the ink are connected into a sample-spanning colloidal network. The connections between the sheets are likely weak physical bonds (e.g., van der Waals interactions), which can be broken once the imposed shear exceeds the yield stress. At this point, the sample flows, exhibiting shear-thinning behavior in steady shear (i.e., the viscosity decreases as the shear rate increases) (Figure 3c). An estimate of the yield stress  $\sigma_y$  can be obtained from an oscillatory stress sweep (Figure 3e), which is a plot of  $G'$



**Figure 3.** Extrusion-based 3D printed ink properties and hierarchically porous hGO mesh architecture. a) Scheme showing the components (hGO, H<sub>2</sub>O) used to create the aqueous and additive-free 3D printable ink. b) Digital image of the aqueous hGO ink loaded into a printing syringe. c–e) Rheological properties of the hGO ink showing that the ink is solid-like at rest (i.e., has a yield stress) and exhibits shear-thinning behavior with increasing shear. An estimate of the yield stress is obtained from the data in (d):  $\sigma_y \approx 500$  Pa. f) Digital image showing the process of printing complex 3D architectures line-by-line. g) Isometric view of the printed hGO mesh (0.8 mm line spacing) after lyophilization. h) Optical image showing a top-down view of the freeze-dried hGO mesh structure. Scale bar is 500  $\mu\text{m}$ . i–l) Cross-sectional SEM images of the hierarchically porous 3D printed hGO mesh structure: hGO sheets are nanoporous (4–25 nm holes), lyophilization creates tens of micrometer-sized pores on the printed filaments and the printed mesh structure possesses <500  $\mu\text{m}$  square pores. Note that the hGO sheets are layered along the extruding direction due to the printing procedure, as shown in (l). Scale bars in (j) and (k) are 50  $\mu\text{m}$  while (i) and (l) are 250  $\mu\text{m}$  and 10  $\mu\text{m}$ , respectively.

and  $G''$  against the stress-amplitude (at a constant frequency of 6.283  $\text{rad s}^{-1}$ ). At low stresses,  $G'$  is constant and higher than  $G''$ , but at a stress around  $\sigma_y = 500$  Pa (dotted line),  $G'$  sharply drops and eventually falls below  $G''$ . This means that the sample behaves like a solid below  $\sigma_y$ , whereas it flows like a liquid above  $\sigma_y$ . Note that the stresses applied during extrusion are orders of magnitude higher than  $\sigma_y$ , allowing the ink to flow through the nozzle (Figure 3b). Once the applied stress is removed (i.e., when the ink is deposited on the surface), it regains its solid-like character.

For extrusion-based 3D printing, the aqueous hGO ink was loaded into a syringe with a 203.2  $\mu\text{m}$  tip diameter (Figure 3b) and dispensed into fine lines in a layer-by-layer arrangement on a glass substrate by adjusting the compressed air pressure and printing rate (Figure 3f,g). Due to the viscoelastic behavior of the ink, multiple extruded hGO layers can be stacked together to create complex 3D printed architectures such as mesh structures (Figure 3h,i). Conversely, additive-free, aqueous inks with (hydrophobic) hG do not have the proper

- *Binderless & additive-free* 3D printable ink
- *Hydrophilic hGO in H<sub>2</sub>O* (~100 mg/mL)  
→ Homogeneously mix the ink with mortar & pestle and load into syringe

rheology and composition to print and retain fine filaments on glass. After the desired structure is printed, an overnight freeze drying or lyophilization process is employed to remove the remaining H<sub>2</sub>O and preserve the 3D printed architecture. The hGO mesh (0.6 cm  $\times$  0.6 cm) consists of six printed zigzag structures (0.8 mm line spacing) stacked on top of each other to create a trilayer mesh structure. Figure 3h is a top-down optical microscopy image of the freeze-dried hGO mesh with extrusion printed lines and columns. This 3D printed hGO architecture is inherently macroporous due to the open mesh structure with <0.5 mm wide square pores.

Directly after lyophilization, the detailed structure and porosity of the hGO mesh were also studied via scanning electron microscopy (SEM) (Figure 3i–l). Figure 3i is a cross-sectional SEM image of the trilayer hGO mesh structure taken directly after the printing and lyophilization procedures without further modification. Tens of micrometer-sized pores decorate the printed mesh layers which are likely introduced due to the freeze drying procedure. In this way, it is evident

that the 3D printed hGO mesh possesses microscale porosity (Figure 3j–l). Due to the nanoporous nature of the hGO sheets, the 3D printed hGO mesh displays trimodal porosity: 4–25 nm through-holes on hGO sheets, lyophilization-induced tens of micrometer-sized pores on the printed filaments and <500  $\mu\text{m}$  square pores of the printed mesh design. Additionally, as the viscoelastic hGO ink is dispensed through the syringe, the hGO sheets become oriented in a layered fashion along the extruding direction. Figure 3l displays the stacked hGO sheet configuration within the printed filaments.

Hierarchically porous 3D architectures are promising in a wide range of applications, especially energy storage devices (batteries, supercapacitors) that rely on facile ionic/mass transport and interfacial reactions to function. To demonstrate the unique porosity attained in the 3D printed structure, the meshes were employed as advanced battery electrodes. Specifically, the hierarchically porous 3D printed hGO mesh has an ideal structure for Li–O<sub>2</sub> batteries where surface reactions with gas-phase oxygen facilitate reversible oxygen reduction (ORR) and evolution (OER) reactions.<sup>[36,37]</sup> In this way, the triporous nature of the hGO mesh should allow oxygen and electrolyte to access the entire printed structure, which opens up mass and ionic transfer pathways within the 3D printed Li–O<sub>2</sub> electrode to enhance overall electrochemical performance. To the best of our knowledge, this is the first time a 3D printed cathode has been demonstrated for Li–O<sub>2</sub> batteries.

To verify the aforementioned hypothesis, the hGO mesh structures were thermally reduced at 1000 °C in an argon-filled tube furnace for use as Li–O<sub>2</sub> cathodes. The reduced hGO (r-hGO) mesh Li–O<sub>2</sub> cathodes were then assembled into CR2032 coin cells against a lithium metal counter/reference electrode and placed into a custom-made, sealed electrochemical setup prior to oxygen gas purging (see Materials and Methods section in the Supporting Information). Figure 4a displays the deep discharge performance of the 3D printed r-hGO mesh tested at 0.1 mA cm<sup>-2</sup> with a remarkable areal capacity of 13.3 mA h cm<sup>-2</sup> ( $\approx 4.8$  mA h in total capacity or  $\approx 3879$  mA h g<sup>-1</sup>). Note that previous reports in the literature on porous carbon and GO-based Li–O<sub>2</sub> cathodes range in performance (from  $\approx 600$  mA h g<sup>-1</sup> to >10 000 mA h g<sup>-1</sup>; areal capacity is typically not reported) based on the type of cathode material/structure and specific processing conditions.<sup>[38–40]</sup> For comparison, vacuum filtrated (VF) films using the same synthesized hGO material (with identical areal dimensions) were fabricated, dried, thermally reduced, assembled, and then tested in CR2032 coin cells under the same current density. The morphology and structure of the dense VF r-hGO films can be found in the Supporting Information, where the nature of the filtration process affects the porosity induced by the (freeze) drying procedure (Figure S3, Supporting Information). In this case, the full discharge areal capacity was a mere 0.21 mA h cm<sup>-2</sup> (<0.03 mA h in total capacity or  $\approx 92$  mA h g<sup>-1</sup>).

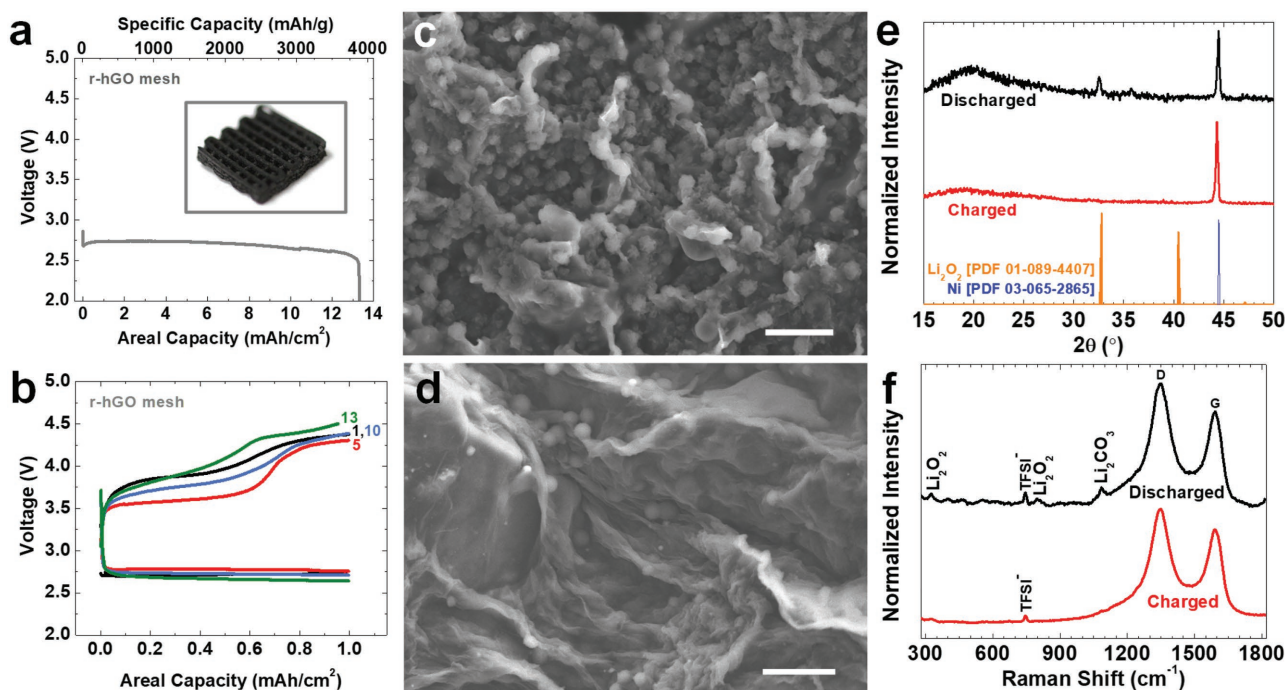


**Figure 4.** Electrochemical performance and postcharacterization of 3D printed Li–O<sub>2</sub> cathodes comprised of hierarchically porous r-hGO mesh architectures. a) Deep discharge performance of the r-hGO mesh, which demonstrates the hierarchical porosity of the 3D printed mesh cathode. Note that the specific capacity reported in (a) is mA h g<sup>-1</sup><sub>sample</sub> not mA h g<sup>-1</sup><sub>carbon</sub>. b) Controlled discharge–charge cycling depths (1 mA h cm<sup>-2</sup>) for the r-hGO mesh at 0.1 mA cm<sup>-2</sup>. SEM images of disassembled r-hGO mesh cathodes in the c) discharge and d) charge state. Spherical 1  $\mu\text{m}$  Li<sub>2</sub>O<sub>2</sub> particles completely cover the r-hGO mesh during the discharge process. Due to the absence of catalyst, some Li<sub>2</sub>O<sub>2</sub> particles remain embedded between the layered r-hGO sheets upon recharging. Scale bars in (c) and (d) are 5  $\mu\text{m}$ . e) XRD and f) Raman spectra of r-hGO mesh cathodes in the discharge and charge state, which verifies the main discharge product is Li<sub>2</sub>O<sub>2</sub>.

due to the film's 2D structure, which severely limits the surface-based reactions required for Li–O<sub>2</sub> battery operation (Figure S4, Supporting Information). This significant capacity difference (by a factor exceeding 63 and 42 in terms of mA h cm<sup>-2</sup> and mA h g<sup>-1</sup>, respectively) demonstrates the architectural advantage of the r-hGO mesh fabricated by the extrusion-based 3D printing procedure and subsequent processing steps (i.e., lyophilization). SEM images of the dense VF r-hGO film show a lack of micro-sized (and macroscale) pores which reduces the cathode's accessible surface area, inhibits mass/ionic transport and limits the attainable capacity under the full discharge condition (Figure S3, Supporting Information). The cycling performance of the 3D printed r-hGO mesh and VF r-hGO film cathodes under controlled discharge–charge depths of 1 mA h cm<sup>-2</sup> are shown in Figure 4b and Figure S4 (Supporting Information), respectively. The r-hGO mesh cycles for ≈13 cycles at 0.1 mA cm<sup>-2</sup> before reaching the upper voltage limit of 4.5 V however, the VF r-hGO film does not complete even one full cycle under the same testing conditions. Therefore, the hierarchical porosity of the 3D printed mesh architecture is advantageous in terms of enhancing Li–O<sub>2</sub> battery performance including capacity retention and cyclability.

The 3D printed r-hGO mesh cathodes in the discharge and charge states (at a curtailed depth of 1 mA h cm<sup>-2</sup>) were disassembled and characterized further by microscopy, spectroscopy, and X-ray diffraction (XRD) techniques to verify the main discharge product: lithium peroxide (Li<sub>2</sub>O<sub>2</sub>). Figure 4c,d displays SEM images of the discharged and charged r-hGO cathodes, respectively. It was previously demonstrated that the discharge products, such as Li<sub>2</sub>O<sub>2</sub>, preferentially form near the surface adjacent to the air/oxygen side due to the oxygen diffusion gradient within dense and thick hG-based dry compressed air cathodes.<sup>[23]</sup> Here, it appears that during discharge, spherical 1 μm particles are uniformly distributed through the entire electrode thickness, which suggests more efficient oxygen diffusion within the porous 3D mesh architecture (Figure 4c). Upon recharging, the flakes that comprise the r-hGO mesh become visible; however, some particles remain embedded between the layered hGO sheets (Figure 4d). To confirm the identity of the 1 μm particles, XRD and Raman spectroscopy were employed on both discharged and charged r-hGO mesh cathodes (Figure 4e,f). Note that all postcharacterization techniques were conducted on r-hGO meshes with the attached Ni metal foam and thus, peak identification for Ni [PDF 03-065-2865] was included in the following XRD spectra. Unlike the charged r-hGO mesh, the discharged cathode displays a distinct peak at 2θ ≈ 32.6°, which is indicative of Li<sub>2</sub>O<sub>2</sub> [PDF 01-089-4407] (Figure 4e). The Raman spectra shown in Figure 4f also confirm Li<sub>2</sub>O<sub>2</sub> formation and decomposition during the discharge and charge processes, respectively. In the discharge state, multiple peaks for Li<sub>2</sub>O<sub>2</sub> as well as lithium carbonate (Li<sub>2</sub>CO<sub>3</sub>) and the lithium salt anion (TFSI<sup>-</sup>) are observed. Upon recharging, both the Li<sub>2</sub>O<sub>2</sub> and Li<sub>2</sub>CO<sub>3</sub> peaks disappear while some leftover salt remained on each 3D printed cathode. Therefore, the main discharge product for the 3D printed r-hGO mesh Li–O<sub>2</sub> cathodes is confirmed as Li<sub>2</sub>O<sub>2</sub>.

To further enhance the materials' electrocatalytic activity and facilitate a more reversible ORR/OER,<sup>[36,41]</sup> nanosized catalysts were introduced on the 3D printed r-hGO mesh surface.

Previously, ruthenium (Ru)-based nanocatalysts have been shown to exhibit excellent OER performance in Li–O<sub>2</sub> batteries.<sup>[42–46]</sup> The r-hGO mesh was first soaked in a precursor Ru salt solution followed by chemical reduction using aqueous sodium borohydride to achieve a catalyst-decorated architecture. Figure S5 of the Supporting Information illustrates that ≈10 nm nanoparticles uniformly decorate the r-hGO mesh after the unoptimized catalyst loading procedure. Elemental mapping and X-ray photoelectron spectroscopy (XPS) confirmed the composition of the metallic Ru nanoparticles as well as the relatively low Ru loading (9.6 wt%) for the 3D printed mesh, respectively (Figures S6 and S7, Supporting Information). Notably, the microscale porosity of the r-hGO mesh is preserved after the Ru catalyst loading procedure (Figure S5, Supporting Information). With Ru nanocatalyst, the 3D printed mesh exhibited improved cyclability by twofold compared to the neat r-hGO mesh (Figure S8, Supporting Information).

To further illustrate the importance of hierarchical porosity, trilayer meshes were extrusion printed using different GO-based materials: GO from natural graphite powder as well as GO synthesized from the starting (Vor-X) graphene typically used to create hG. The three GO-based materials (hGO, GO from Vor-X graphene, GO from natural graphite) were first synthesized through liquid-phase oxidation using the simplified or modified Hummer's method (see Materials and Methods section in the Supporting Information). Figure 5a and Figure S2 (Supporting Information) both confirm the presence of tens of nanometer-sized through-holes on the hGO flakes. However, no nanosized holes can be observed for both the GO from Vor-X graphene and GO from natural graphite even at higher TEM magnifications, which confirms that the synthesis processes do not induce porosity when the starting materials (Vor-X graphene, natural graphite) are nonporous (Figure 5b,c; Figures S9 and S10, Supporting Information). Raman and FTIR spectra demonstrate that all GO-based materials reported in this work have a similar level of disorder and contain oxygen-containing functional groups that decorate the basal planes (Figure S11, Supporting Information). XPS results further confirm that each GO-based powder has a similar level of oxidation based on the atomic percentages of carbon and oxygen (Figure S12, Supporting Information). In this case, all GO-based materials are hydrophilic and suitable for aqueous ink dispersions. Additionally, the rheological properties of the additive-free GO-based inks are largely comparable to those of the hGO ink (Figure 5d–f), i.e., all three inks show gel-like (yield stress) behavior. Note that the yield stresses for GO from Vor-X graphene and GO from natural graphite inks exceed the hGO ink potentially due to the lack of nanoporosity in these samples. However, the ink viscosities at high shear-rates are identical for the three materials, which confirm the extrudability and printability of all the aforementioned inks.

Extrusion-based 3D printing was employed to create trilayer mesh structures composed of each GO-based material (mass loading of 5.42 ± 0.24 mg cm<sup>-2</sup>) via the same printing procedure (line spacing, mesh areal dimensions, etc.) (insets of Figures 4a and 5g). After printing and lyophilization, the GO-based meshes were thermally reduced and tested as Li–O<sub>2</sub> battery cathodes. Figure 5g compares the full areal capacity of the nanoporous r-hGO mesh to the mesh cathodes comprised

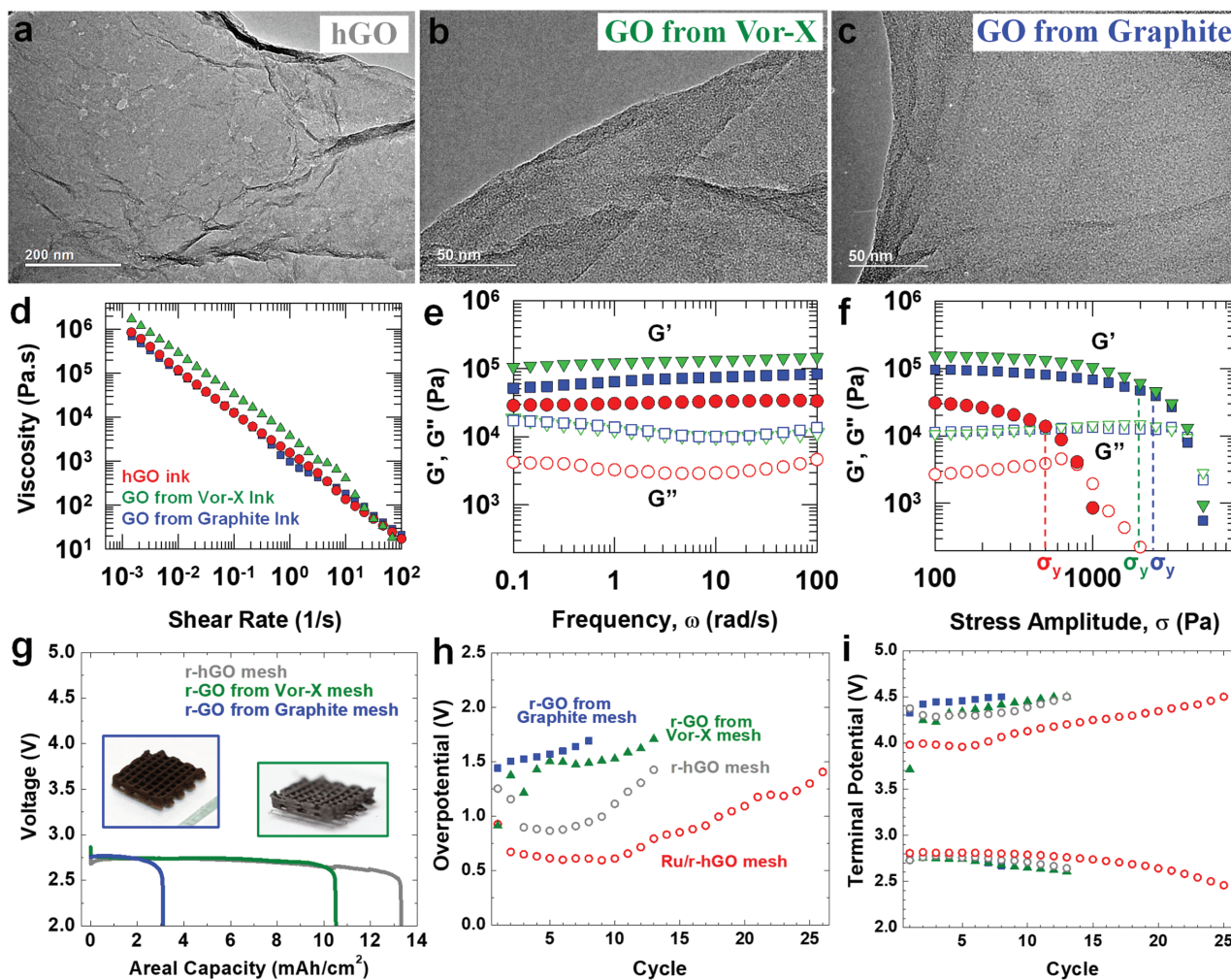


**Figure 5.** Influence of hierarchical porosity: comparison of GO-based materials, inks and 3D printed meshes without nanoholes. TEM images of: a) hGO, b) GO from Vor-X graphene, and c) GO from natural graphite flakes. Unlike hGO, both GO from Vor-X graphene and GO from natural graphite flakes do not possess nanosized through-holes. Rheological measurements of all GO-based inks: hGO (red circles), GO from Vor-X graphene (green triangles), and GO from natural graphite (blue squares): d) Steady-shear data in terms of viscosity versus shear rate. e) Dynamic frequency sweeps showing the elastic ( $G'$ ) and viscous ( $G''$ ) moduli of all inks are frequency independent. f) Dynamic stress sweeps, where  $G'$  and  $G''$  are plotted against the stress-amplitude (at a constant frequency of  $6.283 \text{ rad s}^{-1}$ ). The dotted lines in (f) indicate the yield stress  $\sigma_y$  of each ink sample. The GO from natural graphite ink possesses the highest  $\sigma_y$  ( $\approx 2500 \text{ Pa}$ ) however, the extruding stress still exceeds this value. Thus, each GO-based ink can be readily 3D printed into complex geometries. g) Deep discharge performance of the nanoporous r-hGO mesh as well as mesh cathodes comprised of nonporous GO materials (GO from Vor-X graphene, GO from natural graphite). Plots of h) overpotential and i) discharge/charge terminal potential versus cycle number for all 3D printed Li-O<sub>2</sub> cathodes. The nanoporous hGO-based meshes (with and without Ru loading) show the lowest overpotentials and similar/improved cyclability compared to the other GO-based meshes.

of nonporous GO materials (GO from Vor-X graphene and GO from natural graphite) at a current density of  $0.1 \text{ mA cm}^{-2}$ . The r-GO from natural graphite mesh displayed the lowest capacity values under the full discharge condition ( $3.1 \text{ mA h cm}^{-2}$ ,  $\approx 600 \text{ mA h g}^{-1}$ , or  $0.77 \text{ mA h}$  in total capacity) (Figure 5g; Figure S13, Supporting Information). The r-GO from Vor-X graphene mesh showed a deeper discharge depth of  $10.5 \text{ mA h cm}^{-2}$  ( $2.63 \text{ mA h}$  in total capacity or  $\approx 2471 \text{ mA h g}^{-1}$ ). However, hGO outperformed each GO-based material, which can be attributed to the nanoporous nature of the hGO flakes (Figure 4a; Figure S13, Supporting Information). Note that these full areal capacities are underestimated since the inherent macroporosity of the mesh structures (i.e., the  $<500 \mu\text{m}$  square

pores) were not subtracted out from the overall electrode dimensions before electrochemical testing. Additionally, all specific capacities reported in this work are based on the total electrode mass ( $\text{mA h g}^{-1}_{\text{sample}}$  instead of  $\text{mA h g}^{-1}_{\text{carbon}}$ ). The influence of nanoporosity on electrochemical performance can also be observed in the voltage profiles of each GO-based 3D printed cathode (Figure 4b; Figure S14, Supporting Information). To illustrate this, the overpotential and terminal potentials were plotted against cycle number for each 3D printed GO-based mesh: r-hGO, Ru/r-hGO, r-GO from Vor-X graphene, and r-GO from natural graphite (Figure 5h,i). The Ru/r-hGO mesh exhibited the lowest overpotentials of all GO-based meshes, which correlates to the aforementioned twofold increase in cycle life.

Due to the unoptimized nanosized Ru catalyst, a  $<1$  V overpotential was achieved for nearly 19 cycles. Similarly, the overpotentials for the neat r-hGO mesh cathode from cycles 3 to 9 were also below 1 V unlike the 3D printed meshes composed of GO-based materials without nanoporosity (GO from Vor-X graphene, GO from natural graphite). Additionally, the 3D printed mesh composed of GO from natural graphite exhibits the lowest discharge potentials and the highest charge potentials, which coincides with the cathode's limited full discharge depth and poor cyclability (Figure 5i). The r-hGO and r-GO from Vor-X graphene meshes exhibit nearly identical terminal potentials in the discharge and charge conditions. However, after close inspection, the r-hGO mesh cathode had slightly higher discharge potentials and slightly lower charge potentials. These results demonstrate the importance of hierarchical porosity on the mass transfer (oxygen and electrolyte) and ionic transport pathways within the 3D printed Li-O<sub>2</sub> cathode. Specifically, the nanoholes present on the hGO sheets facilitate improved active site utilization within the 3D printed mesh structure, which enhances overall Li-O<sub>2</sub> battery performance. Future studies can be envisioned where nanoporous materials can be 3D printed into a plethora of structurally conscious electrode designs (beyond mesh structures) to further improve the performance of energy storage devices and beyond.

In summary, a nanoporous GO material (hGO) was synthesized directly from a commercial graphene powder using scalable and purely oxidative processes (i.e., controlled air oxidation to create hG followed by liquid-phase oxidation) for extrusion-based 3D printing of hierarchical porous architectures. Unlike conventional GO materials that rely on additional activation or processing steps (templating, etching, KOH activation, etc.) to introduce porosity, the as-prepared hGO powder is inherently nanoporous with 4–25 nm through-holes due to the unique, nanoporous starting material (hG), and facile processing procedure inspired by the modified Hummer's method. Liquid-phase oxidation via the so-called simplified Hummer's method enables hydrophilicity, which facilitates stable 3D printable ink dispersions in H<sub>2</sub>O without the use of binders or other additives. Due to the viscoelastic behavior, the aqueous and additive-free hGO ink can be readily extruded into advanced, freestanding 3D mesh designs with trimodal porosity: nanoscale (4–25 nm through-holes on hGO sheets), microscale (lyophilization-induced micropores on the printed filaments), and macroscale ( $<500$   $\mu\text{m}$  square pores arise from the printed mesh design).

The hierarchically porous and additive-free hGO meshes were thermally reduced and successfully demonstrated as the first 3D printed Li-O<sub>2</sub> cathodes reported in the literature to illustrate the importance of both porous nanomaterials and structurally conscious electrode designs. Compared to a 2D vacuum filtrated film, the 3D printed mesh's macroscale and microscale porosity enhanced active-site utilization as well as mass/ionic transport to dramatically enhance overall Li-O<sub>2</sub> battery performance (42-fold and 63-fold improvement in full discharge capacity by mass and area, respectively). GO materials lacking nanoholes (GO from Vor-X graphene, GO from natural graphite) were also synthesized and employed as 3D printed Li-O<sub>2</sub> cathodes to investigate the role of hierarchical porosity, specifically nanoporosity, on electrochemical performance. The nanoporous r-hGO mesh outperformed the non-nanoporous

GO-based mesh cathodes under the full discharge condition as well as in terms of cycling depth and stability. Through unoptimized Ru catalyst decoration, the nanoporous r-hGO mesh also displayed improved cyclability by twofold. The results confirm that the macro- and microscale porosity introduced by 3D printing (and the associated processing steps) is the most critical aspect in terms of improving overall air cathode capacity, while nanoporosity due to through-holes can further improve transport pathways (i.e., reduce tortuosity) and enhance performance to a much smaller degree. Thus, this work demonstrates that conscious design and implementation of nanoporous carbon-based 2D materials into freeform and hierarchically porous electrode architectures can enhance the performance of next-generation energy storage systems while providing a potential avenue for AM techniques in advanced battery manufacturing. Note that the nanoporous materials (hGO) as well as the hierarchically porous 3D printed architectures reported in this work are not limited to batteries. Future studies are warranted to expand the library of 3D printed materials and structurally conscious architectures beyond energy storage devices, which could open up new technological opportunities for catalysis, electronics, and thermal management, among many others.

## Supporting Information

Supporting Information is available from the Wiley Online Library or from the author.

## Acknowledgements

This work was supported by the NASA Langley Internal Research and Development (IRAD) Program. S.D.L. acknowledges the support by the Department of Defense (DoD) through the National Defense Science and Engineering Graduate (NDSEG) Fellowship Program. J.T.M. was supported by the Research Experiences for Undergraduates (REU) Program, which was funded in part by the National Science Foundation (NSF) and the Transportation Electrification Grant (#EEC1263063). L.Q.G. was supported by the NASA Langley Aerospace Research Summer Scholars (LARSS) Program. The authors would like to thank Arthur von Wald Cresce for his help and analysis of XPS samples. The authors acknowledge the support of the Maryland NanoCenter and its AIMLab.

## Conflict of Interest

The authors declare no conflict of interest.

## Keywords

3D printing, additive manufacturing, holey graphene oxide, lithium-oxygen batteries, porous electrode architecture

Received: September 28, 2017

Revised: December 17, 2017

Published online: January 30, 2018

[1] K. Sun, T. S. Wei, B. Y. Ahn, J. Y. Seo, S. J. Dillon, J. A. Lewis, *Adv. Mater.* **2013**, *25*, 4539.

- [2] F. Kun, Y. Wang, C. Yan, Y. Yao, Y. Chen, J. Dai, S. Lacey, Y. Wang, J. Wan, T. Li, Z. Wang, Y. Xu, L. Hu, *Adv. Mater.* **2016**, *28*, 2587.
- [3] A. E. Jakus, E. B. Secor, A. L. Rutz, S. W. Jordan, M. C. Hersam, R. N. Shah, *ACS Nano* **2015**, *9*, 4636.
- [4] S. V. Murphy, A. Atala, *Nat. Biotechnol.* **2014**, *32*, 773.
- [5] B. C. Gross, J. L. Erkal, S. Y. Lockwood, C. P. Chen, D. M. Spence, *Anal. Chem.* **2014**, *86*, 3240.
- [6] S. K. Moon, Y. E. Tan, J. Hwang, Y. J. Yoon, *Int. J. Precis. Eng. Manuf.: Green Technol.* **2014**, *1*, 223.
- [7] C. Zhu, T. Liu, F. Qian, W. Chen, S. Chandrasekaran, B. Yao, Y. Song, E. B. Duoss, J. D. Kuntz, C. M. Spadaccini, M. A. Worsley, Y. Li, *Nano Today* **2017**, *15*, 107.
- [8] S. Naficy, R. Jalili, S. H. Aboutalebi, R. A. Gorkin, K. Konstantinov, P. C. Innis, G. M. Spinks, P. Poulin, G. G. Wallace, *Mater. Horiz.* **2014**, *1*, 326.
- [9] J. H. Kim, W. S. Chang, D. Kim, J. R. Yang, J. T. Han, G. W. Lee, J. T. Kim, S. K. Seol, *Adv. Mater.* **2015**, *27*, 157.
- [10] Y. W. Zhu, S. Murali, W. W. Cai, X. S. Li, J. W. Suk, J. R. Potts, R. S. Ruoff, *Adv. Mater.* **2010**, *22*, 3906.
- [11] Q. Zhang, F. Zhang, S. P. Medarametla, H. Li, C. Zhou, D. Lin, *Small* **2016**, *12*, 1702.
- [12] C. Zhao, C. Y. Wang, R. Gorkin, S. Beirne, K. W. Shu, G. G. Wallace, *Electrochem. Commun.* **2014**, *41*, 20.
- [13] G. Z. Sun, J. An, C. K. Chua, H. C. Pang, J. Zhang, P. Chen, *Electrochem. Commun.* **2015**, *51*, 33.
- [14] T. Nathan-Walteser, I. M. Lazar, M. Fabritius, F. J. Tolle, Q. Xia, B. Bruchmann, S. S. Venkataraman, M. G. Schwab, R. Mulhaupt, *Adv. Funct. Mater.* **2014**, *24*, 4706.
- [15] C. Zhu, T. Liu, F. Qian, T. Y. Han, E. B. Duoss, J. D. Kuntz, C. M. Spadaccini, M. A. Worsley, Y. Li, *Nano Lett.* **2016**, *16*, 3448.
- [16] T. Liu, C. Zhu, T. Kou, M. A. Worsley, F. Qian, C. Condes, E. B. Duoss, C. M. Spadaccini, Y. Li, *ChemNanoMat* **2016**, *2*, 635.
- [17] S. Lawes, A. Riese, Q. Sun, N. C. Cheng, X. L. Sun, *Carbon* **2015**, *92*, 150.
- [18] K. Fu, Y. G. Yao, J. Q. Dai, L. B. Hu, *Adv. Mater.* **2017**, *29*, 20.
- [19] X. G. Han, M. R. Funk, F. Shen, Y. C. Chen, Y. Y. Li, C. J. Campbell, J. Q. Dai, X. F. Yang, J. W. Kim, Y. L. Liao, J. W. Connell, V. Barone, Z. F. Chen, Y. Lin, L. B. Hu, *ACS Nano* **2014**, *8*, 8255.
- [20] Y. Lin, X. G. Han, C. J. Campbell, J. W. Kim, B. Zhao, W. Luo, J. Q. Dai, L. B. Hu, J. W. Connell, *Adv. Funct. Mater.* **2015**, *25*, 2920.
- [21] J. T. Xu, Y. Lin, J. W. Connell, L. M. Dai, *Small* **2015**, *11*, 6179.
- [22] S. Lacey, E. Walsh, E. Hitz, J. Dai, J. Connell, L. Hu, Y. Lin, *Nano Energy* **2016**, *31*, 386.
- [23] Y. Lin, B. Moitoso, C. Martinez-Martinez, E. D. Walsh, S. D. Lacey, J. W. Kim, L. M. Dai, L. B. Hu, J. W. Connell, *Nano Lett.* **2017**, *17*, 3252.
- [24] J. Shui, Y. Lin, Y. Xue, J. W. Connell, L. Dai, *ACS Energy Lett.* **2016**, *1*, 260.
- [25] L. Qie, Y. Lin, J. W. Connell, J. T. Xu, L. M. Dai, *Angew. Chem., Int. Ed.* **2017**, *56*, 6970.
- [26] E. D. Walsh, X. G. Han, S. D. Lacey, J. W. Kim, J. W. Connell, L. B. Hu, Y. Lin, *ACS Appl. Mater. Interfaces* **2016**, *8*, 29478.
- [27] Y. X. Xu, Z. Y. Lin, X. Zhong, X. Q. Huang, N. O. Weiss, Y. Huang, X. F. Duan, *Nat. Commun.* **2014**, *5*, 8.
- [28] Q. Q. Zhou, M. Zhang, J. Chen, J. D. Hong, G. Q. Shi, *ACS Appl. Mater. Interfaces* **2016**, *8*, 20741.
- [29] Y. Y. Peng, Y. M. Liu, J. K. Chang, C. H. Wu, M. D. Ger, N. W. Pu, C. L. Chang, *Carbon* **2015**, *81*, 347.
- [30] X. Zhao, C. M. Hayner, M. C. Kung, H. H. Kung, *ACS Nano* **2011**, *5*, 8739.
- [31] H. T. Sun, L. Mei, J. F. Liang, Z. P. Zhao, C. Lee, H. L. Fei, M. N. Ding, J. Lau, M. F. Li, C. Wang, X. Xu, G. L. Hao, B. Papandrea, I. Shakir, B. Dunn, Y. Huang, X. F. Duan, *Science* **2017**, *356*, 599.
- [32] X. G. Han, Z. Yang, B. Zhao, S. Z. Zhu, L. H. Zhou, J. Q. Dai, J. W. Kim, B. Y. Liu, J. W. Connell, T. Li, B. Yang, Y. Lin, L. B. Hu, *ACS Nano* **2017**, *11*, 3189.
- [33] D. C. Marcano, D. V. Kosynkin, J. M. Berlin, A. Sinitskii, Z. Z. Sun, A. Slesarev, L. B. Alemany, W. Lu, J. M. Tour, *ACS Nano* **2010**, *4*, 4806.
- [34] E. Gacia-Tunon, S. Barg, J. Franco, R. Bell, S. Eslava, E. D'Elia, R. C. Maher, F. Guitian, E. Saiz, *Adv. Mater.* **2015**, *27*, 1688.
- [35] C. Zhu, T. Y. Han, E. B. Duoss, A. M. Golobic, J. D. Kuntz, C. M. Spadaccini, M. A. Worsley, *Nat. Commun.* **2015**, *6*, 6962.
- [36] W. B. Luo, X. W. Gao, S. L. Chou, Y. M. Kang, J. Z. Wang, H. K. Liu, S. X. Dou, *Adv. Energy Mater.* **2017**, *2*, 1700234.
- [37] P. G. Bruce, S. A. Freunberger, L. J. Hardwick, J. M. Tarascon, *Nat. Mater.* **2012**, *11*, 19.
- [38] R. Padbury, X. Zhang, *J. Power Sources* **2011**, *196*, 4436.
- [39] M. M. Storm, M. Overgaard, R. Younesi, N. E. A. Reeler, T. Vosch, U. G. Nielsen, K. Edstrom, P. Norby, *Carbon* **2015**, *85*, 233.
- [40] T. Cetinkaya, S. Ozcan, M. Uysal, M. O. Guler, H. Akbulut, *J. Power Sources* **2014**, *267*, 140.
- [41] Y. Y. Shao, S. Park, J. Xiao, J. G. Zhang, Y. Wang, J. Liu, *ACS Catal.* **2012**, *2*, 844.
- [42] X. Y. Zeng, C. H. You, L. M. Leng, D. Dang, X. C. Qiao, X. H. Li, Y. W. Li, S. J. Liao, R. R. Adzic, *J. Mater. Chem. A* **2015**, *3*, 11224.
- [43] H. G. Jung, Y. S. Jeong, J. B. Park, Y. K. Sun, B. Scrosati, Y. J. Lee, *ACS Nano* **2013**, *7*, 3532.
- [44] B. Sun, P. Munroe, G. X. Wang, *Sci. Rep.* **2013**, *3*, 7.
- [45] Z. Y. Guo, D. D. Zhou, H. J. Liu, X. L. Dong, S. Y. Yuan, A. S. Yu, Y. G. Wang, Y. Y. Xia, *J. Power Sources* **2015**, *276*, 181.
- [46] B. Sun, X. D. Huang, S. Q. Chen, P. Munroe, G. X. Wang, *Nano Lett.* **2014**, *14*, 3145.

# ADVANCED MATERIALS

## Supporting Information

for *Adv. Mater.*, DOI: 10.1002/adma.201705651

### Extrusion-Based 3D Printing of Hierarchically Porous Advanced Battery Electrodes

*Steven D. Lacey, Dylan J. Kirsch, Yiju Li, Joseph T. Morgenstern, Brady C. Zarket, Yonggang Yao, Jiaqi Dai, Laurence Q. Garcia, Boyang Liu, Tingting Gao, Shaomao Xu, Srinivasa R. Raghavan, John W. Connell, Yi Lin,\* and Liangbing Hu\**

## Supporting Information

### Extrusion-based 3D Printing of Hierarchically Porous Advanced Battery Electrodes

Steven D. Lacey<sup>a</sup>, Dylan J. Kirsch<sup>a</sup>, Yiju Li<sup>a</sup>, Joseph T. Morgenstern<sup>a</sup>, Brady C. Zarket<sup>b</sup>, Yonggang Yao<sup>a</sup>, Jiaqi Dai<sup>a</sup>, Laurence Q. Garcia<sup>c</sup>, Boyang Liu<sup>a</sup>, Tingting Gao<sup>a</sup>, Shaomao Xu<sup>a</sup>, Srinivasa R. Raghavan<sup>b</sup>, John W. Connell<sup>c</sup>, Yi Lin<sup>d,\*</sup>, Liangbing Hu<sup>a,\*</sup>

<sup>a</sup>Department of Materials Science and Engineering, University of Maryland, College Park, MD 20742-4111, USA

<sup>b</sup>Department of Chemical and Biomolecular Engineering, University of Maryland, College Park, MD, 20742-4111, USA

<sup>c</sup>Advanced Materials and Processing Branch, NASA Langley Research Center, Mail Stop 226, Hampton, VA 23681-2199, USA

<sup>d</sup>National Institute of Aerospace, 100 Exploration Way, Hampton, VA 23666-6147, USA

\*Correspondence to Yi Lin and Liangbing Hu: [yi.lin-1@nasa.gov](mailto:yi.lin-1@nasa.gov); [binghu@umd.edu](mailto:binghu@umd.edu)

### Materials & Methods

*Synthesis of holey graphene (hG):* The hG starting material was prepared by a facile one-step oxidation procedure developed in our laboratories. Approximately 1.5 g of commercial graphene powder (Vor-X, Vorbeck Materials; grade, reduced 070; lot, BK-77x) was placed in an alumina boat and heated to 430°C at 10°C min<sup>-1</sup> in an open-ended tube furnace (OTF-1200X, MTI Corporation). After a 10h hold at 430°C, the as-prepared hG (bulk density of ~6 mg cm<sup>-3</sup>) was obtained and used directly to synthesize hGO via liquid-phase oxidation.

*Synthesis of holey graphene oxide (hGO) & non-nanoporous GO-based materials:* The highly nanoporous hGO (bulk density of 130 mg cm<sup>-3</sup>) was synthesized using an abbreviated version of the modified Hummer's method. This specific liquid-phase oxidation procedure, referred to as the simplified Hummer's method, is described in this work for the first time. First, the as-prepared hG (400 mg), sodium nitrate (200 mg; >99.0% NaNO<sub>3</sub>, Sigma Aldrich) and sulfuric acid (60 mL) were added to a 100 mL flask inside a cold water bath and magnetically stirred for 15 mins. ~600

mg of potassium permanganate (2.4 g in total;  $\text{KMnO}_4$ , low in mercury, ACS, 99.0% min Alfa Aesar) was added to the solution every 5 mins before transferring the flask to a  $\sim 38^\circ\text{C}$  bath. After a 5 h reaction, the flask was left to cool in a cold water bath for 15 mins. Hydrogen peroxide (30%) was then added to the solution in 0.2 mL increments until the residual  $\text{KMnO}_4$  was neutralized. The dark brown solution was centrifuged (3000rpm for 15 mins) a couple times with deionized (DI) water as well as a mixture of hydrochloric acid and DI water. Additional DI centrifuging steps were performed until all the acid was removed from the final hGO product. The hGO material was then freeze-dried (Labconco FreeZone 2.5 Benchtop Freeze Dry System) overnight and directly used to prepare additive-free and aqueous 3D printable inks. Note that the aforementioned simplified Hummer's method can create scalable quantities of hGO ( $>1$  g) by increasing the batch size and subsequent chemical quantities. Additionally, the GO from Vor-X graphene material was synthesized using the simple Hummer's method described in this work; however, the GO from natural graphite was prepared using the conventional modified Hummer's method, which includes mechanical exfoliation of the starting material, graphite, followed by liquid-phase oxidation.

*Ink Preparation & 3D Printing Procedure:* An additive-free and highly concentrated hGO ink ( $\sim 100$  mg  $\text{mL}^{-1}$ ) was prepared by adding DI water to the freeze-dried hGO material. The hGO slurry was mixed thoroughly with a mortar and pestle before placing the ink into a syringe tube with a  $203.2$   $\mu\text{m}$  tip diameter for the printing process. The ink flow was controlled by an air-powered fluid dispenser (DSP501N, Fisnar) and used to print trilayer hGO mesh structures on glass slides with a line spacing of  $0.8$  mm. Note that the nozzle pressure and move speed were altered to achieve optimal printing of the hGO mesh structures with our lab's benchtop 3D printer. After 3D printing, the electrodes were freeze-dried in a Labconco FreeZone 2.5 Benchtop Freeze Dry System to remove the aqueous solvent and retain the printed structure. In terms of scalability

and manufacturing, the relatively slow 3D printing speed (typical speed of  $1 \text{ mm s}^{-1}$  with our benchtop 3D printer) is the limiting factor. However, for industrial purposes, the rheological properties of the reported GO-based inks would likely be tuned to meet the standards of high-throughput manufacturing (i.e. increased printing speed, etc.) and produce the desired complex 3D architectures. Note that freeze drying is widely used industrially (e.g. pharmaceuticals and food) for the scalable production of products and thus, would not be a major challenge from a manufacturing point of view.

*Material Characterization:* Transmission electron microscopy (TEM) and HRTEM images were acquired using a JEM 2100 LaB<sub>6</sub> and a JEM 2100 field emission TEM/STEM microscope, respectively. Scanning electron microscopy (SEM) was conducted on both a Hitachi SU-70 field emission microscope equipped with an energy dispersive spectrometer (EDS) and a TESCAN XEIA3 field emission microscope. A Horiba Jobin Yvon LabRam ARAMIS Raman spectrometer with a 532 nm excitation source was used to obtain the spectra for hG, all GO-based powders and discharged/charged r-hGO meshes. Fourier transform infrared spectroscopy (FTIR) measurements were conducted on a Thermo Nicolet 6700 spectrometer with a DTGS/KBr detector and diamond ATR. Rheological characterization was performed on a TA Instruments AR 2000 stress-controlled rheometer. All steady-shear and dynamic rheological tests were performed utilizing a 20 mm stainless steel parallel plate fixture at 25°C. Dynamic stress sweeps were performed at a constant angular frequency of  $6.283 \text{ rad s}^{-1}$ . Dynamic frequency sweeps were done at a constant strain amplitude within the linear viscoelastic regime of each sample. X-ray photoelectron spectroscopy (XPS) was conducted using a PHI 5000 Versaprobe III scanning XPS microprobe (ULVAC-PHI, Inc.).

*Fabrication of Vacuum Filtrated and Mesh Electrodes:* Vacuum filtrated (VF) hGO films were created by bath sonicating (2.5 h) and ultrasonicating (5 min at 35% amplitude) an hGO solution before pouring into a conventional filtration setup. A vacuum pump filtered out the solution to create a homogeneous hGO film. After removing the PVDF membrane, the freestanding hGO film was dried thoroughly overnight. The 3D printed GO-based meshes (geometric density ranged between  $63.8 \text{ mg cm}^{-3}$  and  $108 \text{ mg cm}^{-3}$ ) were fabricated using the aforementioned printing procedure (see *Ink Preparation & 3D Printing Procedure*). Afterwards, a thermal reduction procedure was employed to fabricate Li-O<sub>2</sub> battery electrodes using all the aforementioned GO-based structures (3D printed meshes & VF films). The 3D printed & VF structures were placed in a closed-end quartz tube furnace. The tube furnace was then purged at room temperature (RT) with a  $100 \text{ mL min}^{-1}$  argon (Ar) flow for 20 mins before thermal reduction at  $1000^\circ\text{C}$  ( $2^\circ\text{C min}^{-1}$  ramp to  $1000^\circ\text{C}$  followed by a 2 h isothermal hold). The reduced (3D printed mesh & VF) structures were stored in a  $105^\circ\text{C}$  vacuum oven overnight before cell assembly.

*Li-O<sub>2</sub> Battery Assembly/Testing:* All CR2032 cells were assembled in an Ar-filled glovebox with the thermally reduced cathode structures against a metallic lithium (Li) foil counter/reference electrode and tested using 1.0 M lithium bis(trifluoromethane)sulfonimide (LiTFSI; Sigma-Aldrich, 99.95%) in dimethyl sulfoxide (DMSO; Sigma-Aldrich,  $\geq 99\%$ ) electrolyte ( $100 \mu\text{L}$  per cell). A 5/8" diameter glass fiber membrane acted as the separator between the Li foil and GO-based cathode; a 5/8" Ni foam cutout between the cathode and air cap acted as an oxygen diffusion layer, current collector, and spacer. Note that the thermally reduced structures (3D printed meshes & 2D VF films) are not flexible, but still robust enough to be handled for battery fabrication. The assembled cells were placed in a custom, air-tight jar with molecular sieves and purged with pure oxygen for at least 10 min before electrochemical measurements. The electrochemical tests were

conducted on a LAND-CT 2001A Battery Testing System. The Li-O<sub>2</sub> cells were cycled under controlled discharge-charge depths of 1 mAh cm<sup>-2</sup> at a current density of 0.1 mA cm<sup>-2</sup> from 2-4.5V. The deep discharge performance of all GO-based cathodes were also tested at 0.1 mA cm<sup>-2</sup>. Note that similar cell assembly and electrochemical testing was performed on the vacuum filtrated (VF) r-hGO films for comparison purposes.

*Ru Calayst Loading Procedure:* The thermally reduced 3D printed electrodes were soaked for 2 h in a 8 mg mL<sup>-1</sup> Ru<sup>3+</sup> solution using ruthenium (III) chloride hydrate (99.9% PGM basis, Ru 38% min, Alfa Aesar) and absolute, anhydrous ethanol. After soaking, an aqueous 0.4 mg mL<sup>-1</sup> sodium borohydride (NaBH<sub>4</sub>) solution was prepared and slowly dropped onto the 3D printed electrodes to induce chemical reduction until no further bubbles were generated. The samples were then dried at 105°C in a vacuum oven overnight.

*Post-Characterization of Disassembled Li-O<sub>2</sub> Cells:* Li-O<sub>2</sub> cells in the discharge and charge states (at a curtailed depth of 1 mAh cm<sup>-2</sup>) were carefully disassembled in an Ar-filled glovebox and tested using microscopic and spectroscopic techniques to determine the type of discharge products. Note that all post-characterization techniques were conducted with the Li-O<sub>2</sub> cathodes attached to Ni metal foam. SEM (Hitachi SU-70 field emission microscope) and Raman (Horiba Jobin Yvon LabRam ARAMIS Raman spectrometer) samples were carefully sealed and transferred to the respective chambers for characterization. A Bruker C2 Discover system with a Cu K $\alpha$  radiation source was employed for X-ray diffraction (XRD) analyses. Before transferring to the XRD system, the disassembled cathode was placed on the sample stage in an Ar-filled glovebox and encapsulated with Kapton tape for protection.

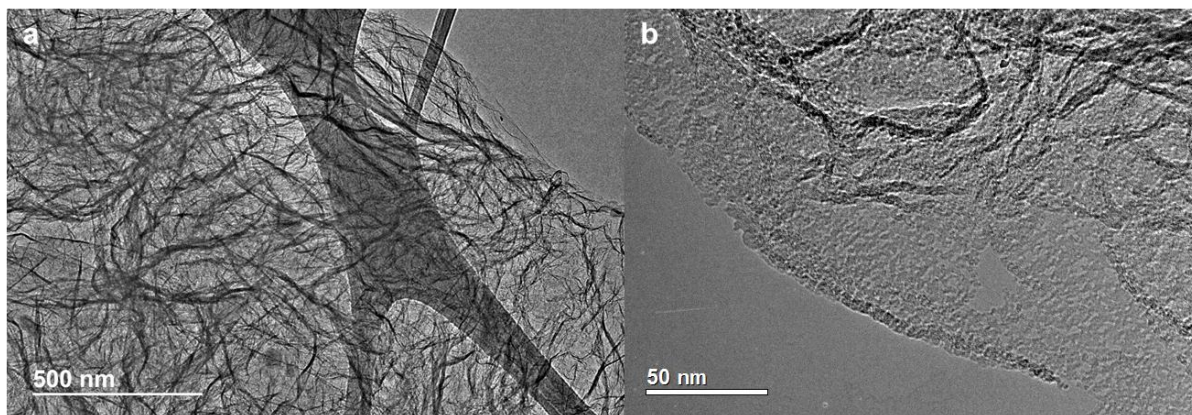


**Figure S1.** TEM images depicting the lateral dimensions of the hG sheets as well as the through-hole size and distribution.

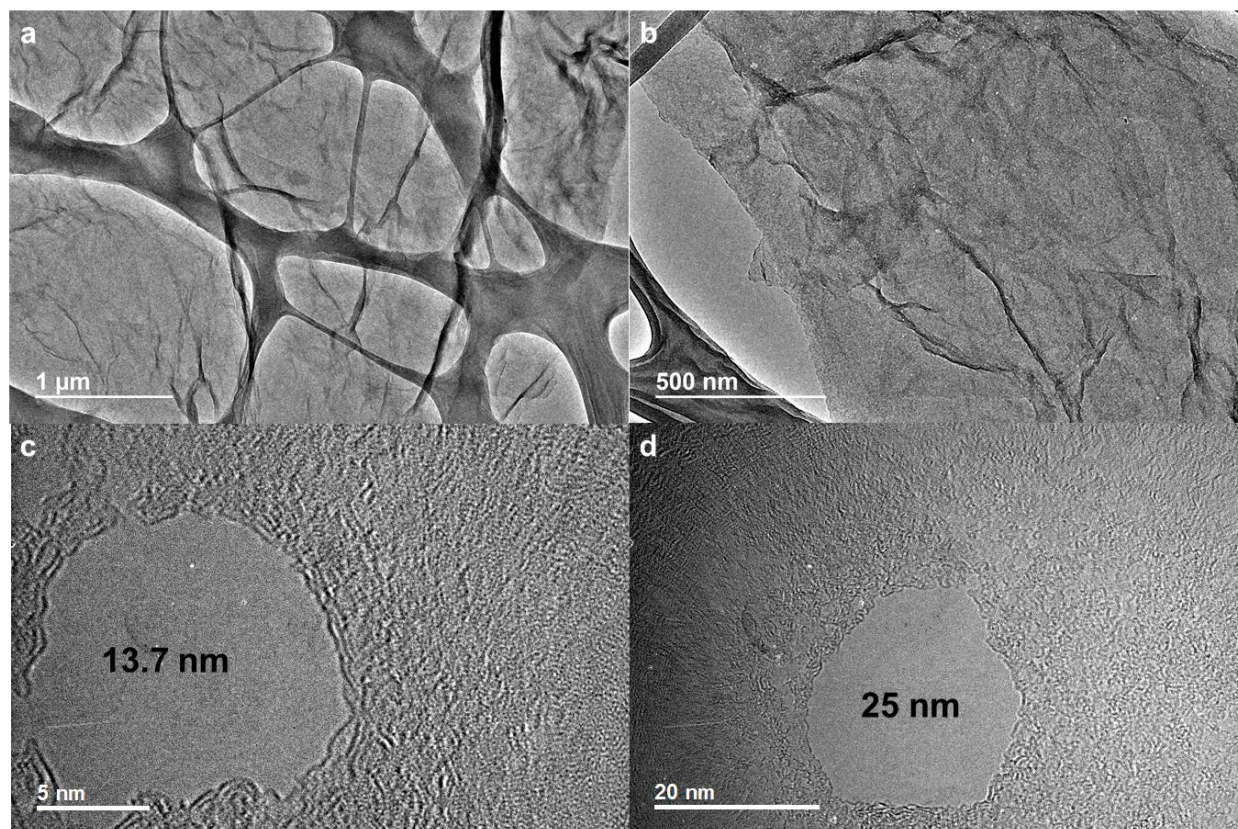


**Figure S2.** TEM images of the highly porous hGO material with (a-b) large lateral sheet dimensions and increased hole sizes compared to the starting hG material. The holes shown in (c)

and (d) are approximately 13.7 nm and 25 nm, respectively, which illustrates the hole diameter distribution of the hGO flakes.

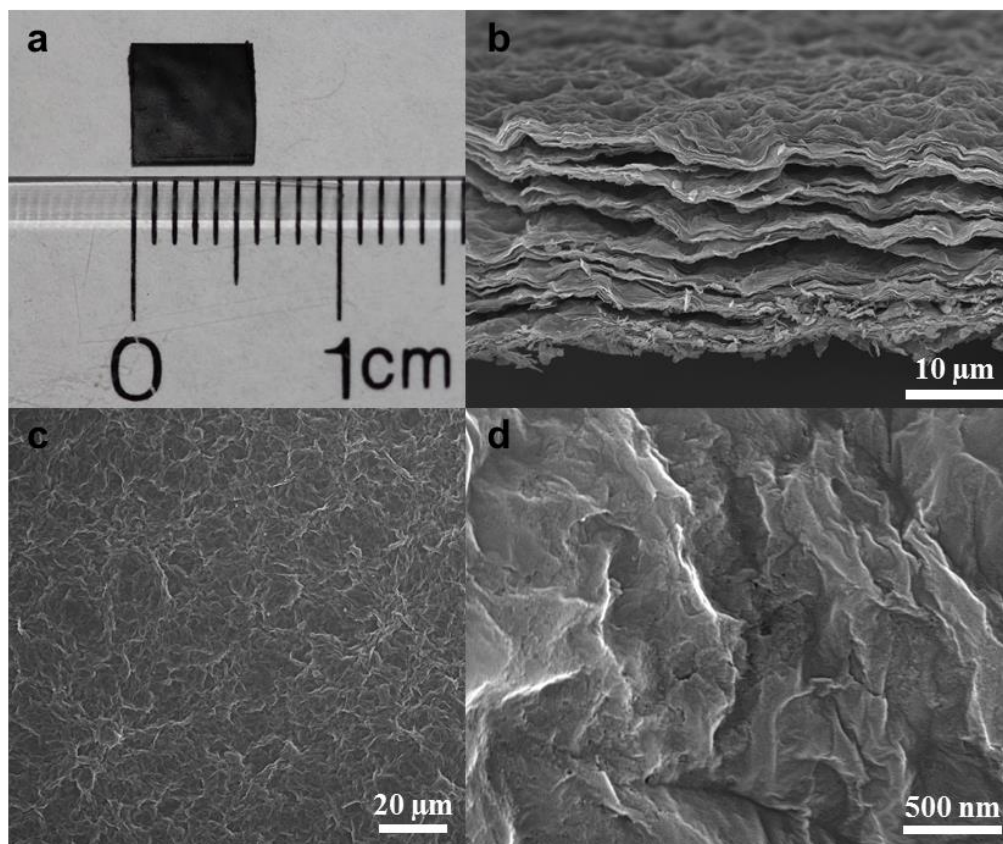


**Figure S3.** (a) Digital image of a vacuum filtrated (VF) hGO film after being cut to size with a razor blade. (b) Cross-sectional SEM image of the VF r-hGO film with a thickness of  $\sim 20 \mu\text{m}$ . SEM images displaying the (c) morphology and (d) hole sizes of the nanoporous VF r-hGO films used as Li-O<sub>2</sub> cathodes. Note that the filtration process results in a dense film with a relatively small amount of water trapped within the structure and thus, the (freeze) drying process does not provide a similar level/density of microsized pores compared to the 3D printed mesh (Figure 3 in the main manuscript).

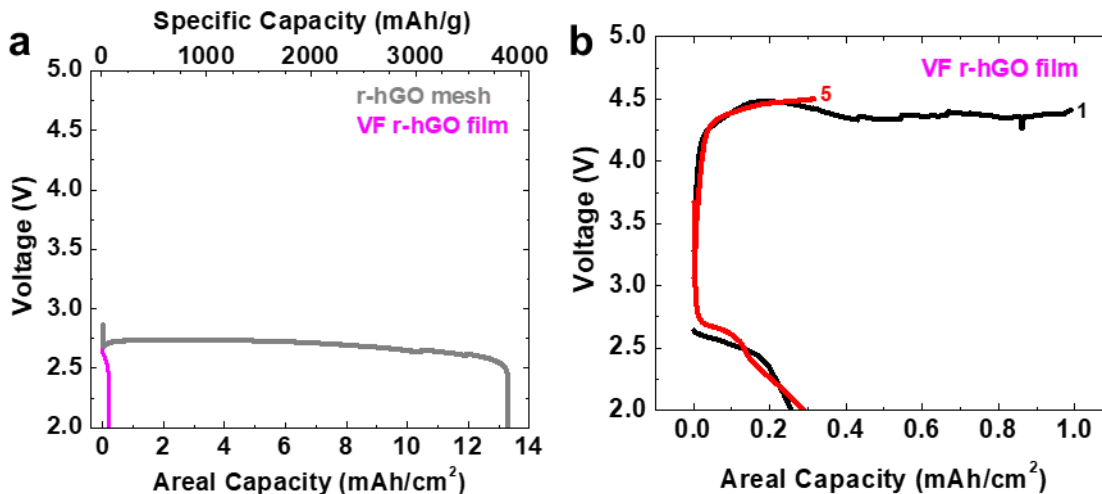


**Figure S4.** (a) Full discharge performance of a VF r-hGO film at  $0.1 \text{ mA cm}^{-2}$ . Compared to the 3D printed mesh, the difference is a factor of  $>63$  and  $>42$  in terms of areal capacity ( $\text{mAh cm}^{-2}$ ) and specific capacity ( $\text{mAh g}^{-1}_{\text{sample}}$ ). This clearly suggests that the micro/macroporosity provided by 3D printing (and the subsequent drying process) is the most critical in terms of capacity improvement of the air cathodes. (b) Cycling performance of a VF r-hGO film, which shows extremely limited capacity retention at the same current density. Note that additional control experiments were performed with different drying processes (freeze drying or oven drying before thermal reduction) however, there were negligible effects on the overall electrochemical performance (full discharge capacity and cyclability) of the VF film cathodes. This is due to the film's 2D structure and the nature of vacuum filtration (i.e. lack of water remaining within the VF film), which limits the accessible surface area ( $78 \text{ m}^2 \text{ g}^{-1}$  from the BJH method) necessary for ORR/OER reactions to occur and further proves that 3D structures are advantageous in terms of improving (Li-O<sub>2</sub>) battery performance.

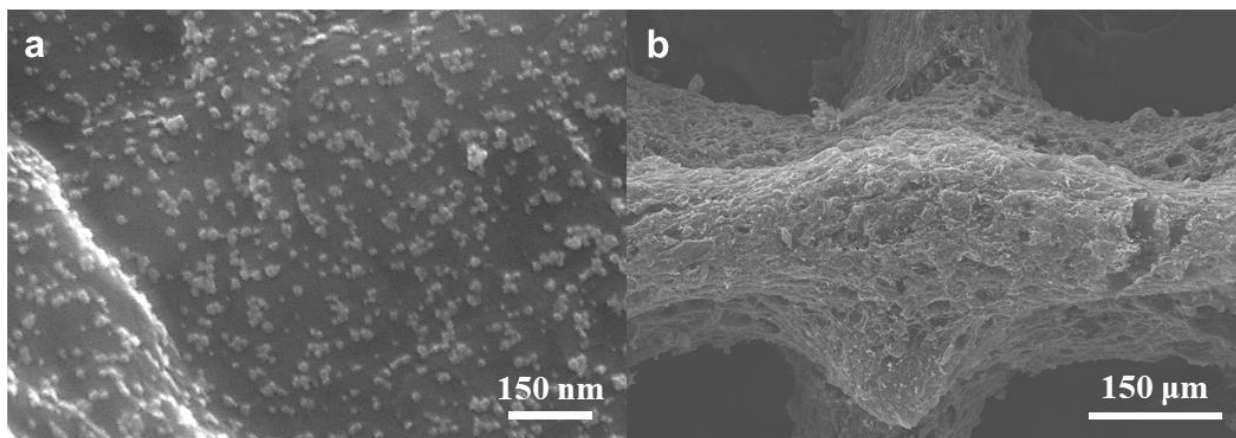


**Figure S5.** SEM images of the Ru/r-hGO mesh with  $\sim 10$  nm particles decorating the flake surface and entire mesh structure. Note that the Ru/r-hGO mesh even after the Ru catalyst loading procedure retains the mesh structure's microscale porosity as shown in (b).

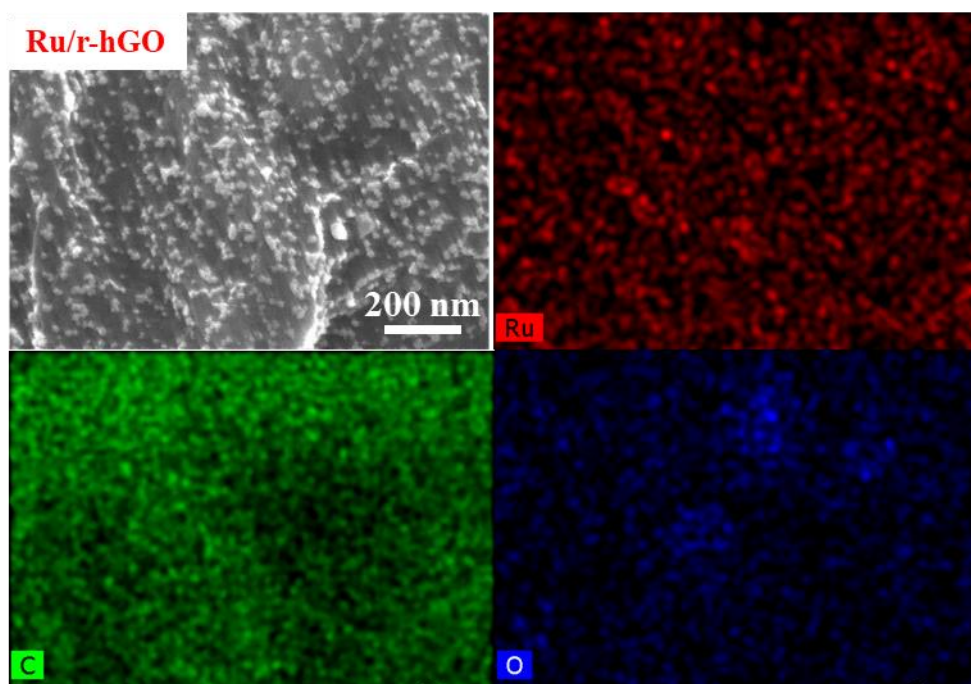


**Figure S6.** SEM/EDS of the 3D printed r-hGO mesh after uniformly loading metallic Ru nanoparticles.

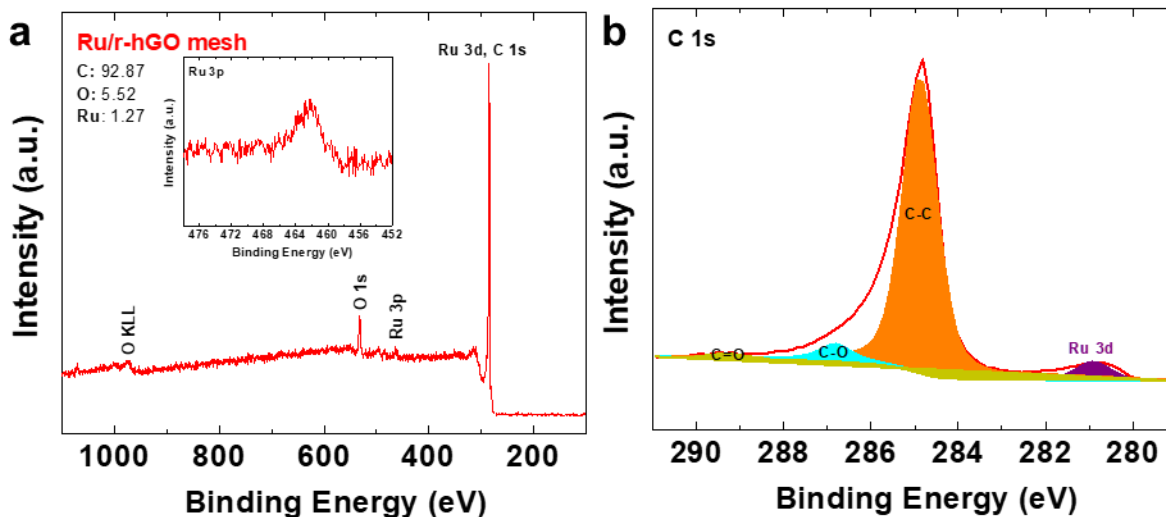


**Figure S7.** XPS compositional analysis of the 3D printed Ru/r-hGO mesh. (a) The full XPS spectra and (b) a higher resolution XPS scan of the C 1s peak, which shows four peaks instead of the typical three peaks for GO. The fourth peak is centered around 281 eV (purple), which corresponds to the Ru 3d<sub>5/2</sub>. The inset in (a) is a higher resolution spectra of the characteristic Ru 3p peak around 462 eV, which verifies the presence of metallic Ru NPs within the Ru/r-hGO mesh. The atomic percentages for C, O, and Ru are shown in (a), which were used to confirm the relatively low Ru loading (9.6 wt%) for the 3D printed mesh.

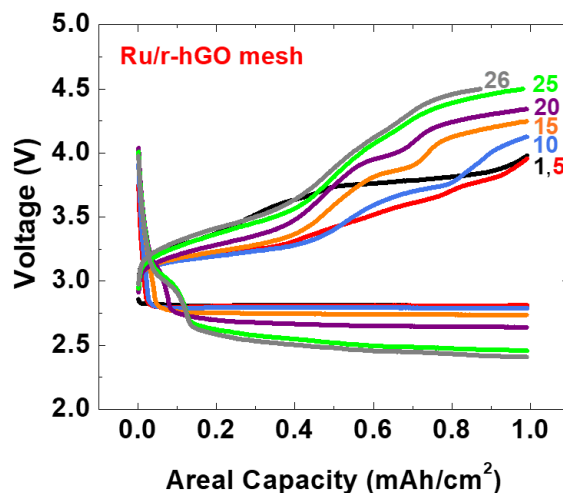


**Figure S8.** Controlled discharge-charge cycling depth (1 mAh cm<sup>-2</sup> at 0.1 mA cm<sup>-2</sup>) for a Ru-decorated 3D printed r-hGO mesh. With unoptimized catalyst loading, the Ru/r-hGO mesh displayed twice the cyclability of the r-hGO mesh.

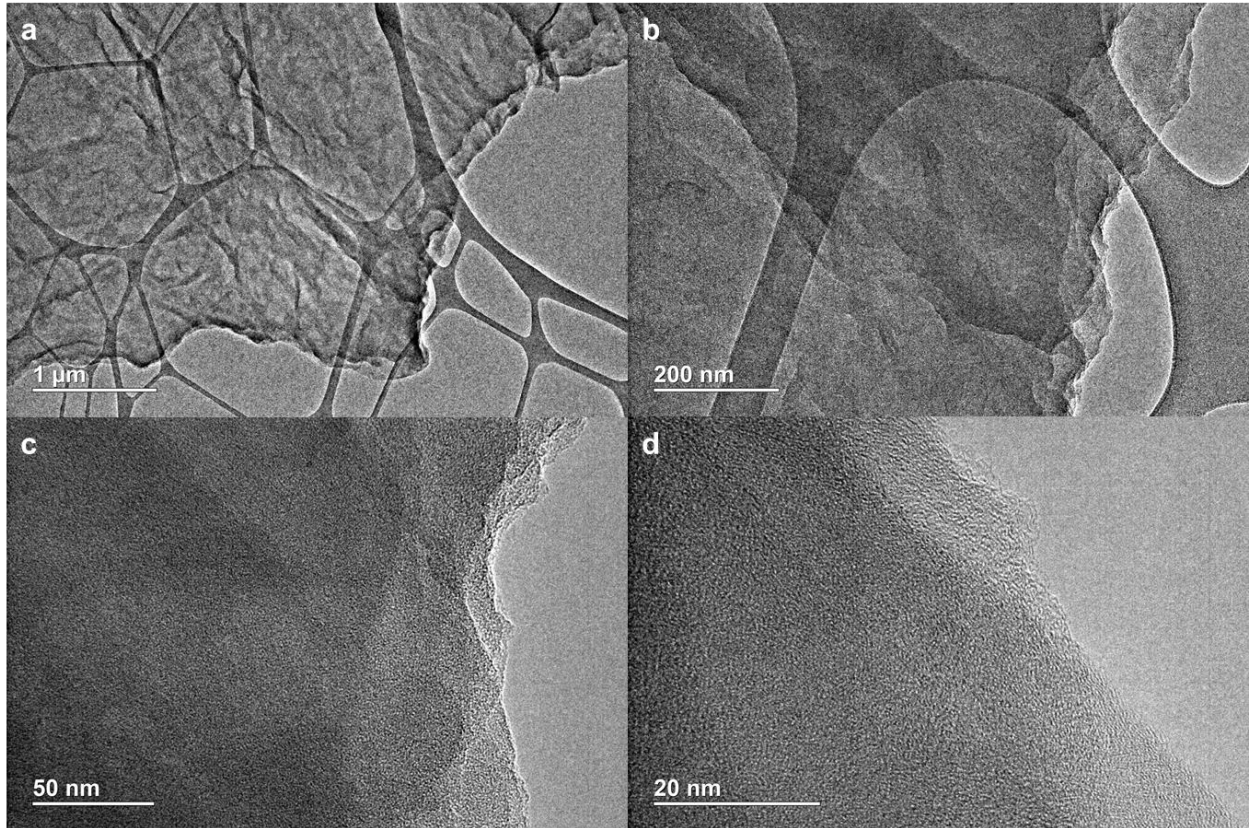


**Figure S9.** TEM images of a non-porous GO material synthesized using the same procedure to create hGO but with a different starting material (i.e. Vor-X graphene instead of hG). The GO from Vor-X flakes have lateral sheet dimensions of several microns or more however, even at high magnifications, no nanosized holes are observed.

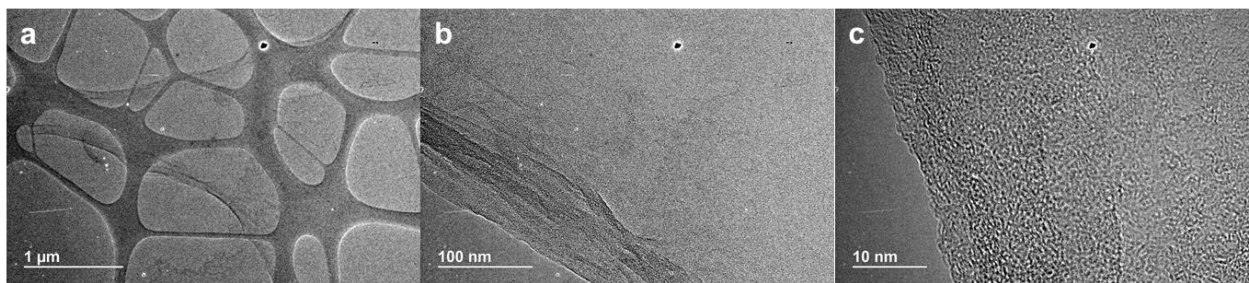


**Figure S10.** TEM images of GO synthesized with natural graphite as the starting material and the conventional modified Hummer's method. Similarly to the GO from Vor-X graphene, the GO from natural graphite flakes do not contain nanosized holes. Note that the dark mark is an artifact present on the CCD camera of the TEM.

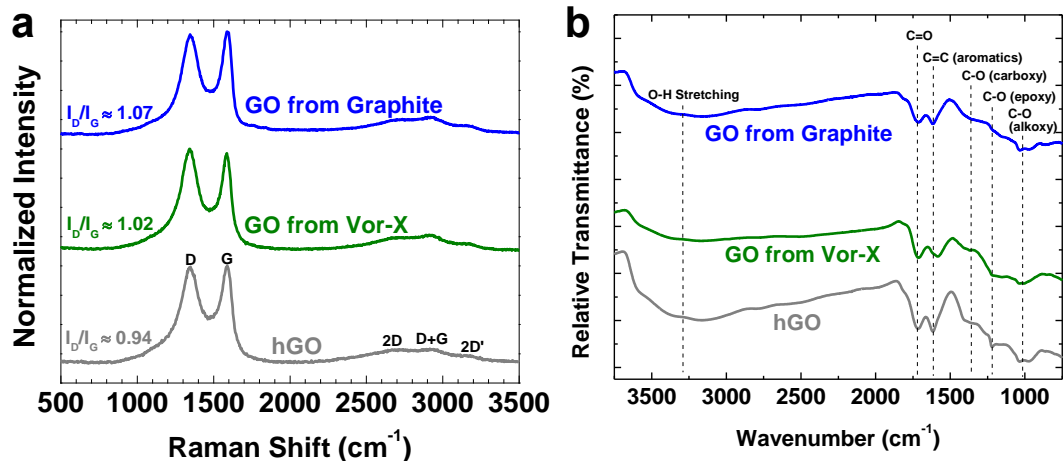


**Figure S11.** (a) Raman and (b) FTIR spectra of all GO-based materials: hGO, GO from Vor-X graphene and GO from natural graphite. The amount of disorder (i.e.  $I_D/I_G$  ratio) and oxygen-containing functional groups are similar between each GO-based material indicative of hydrophilicity.

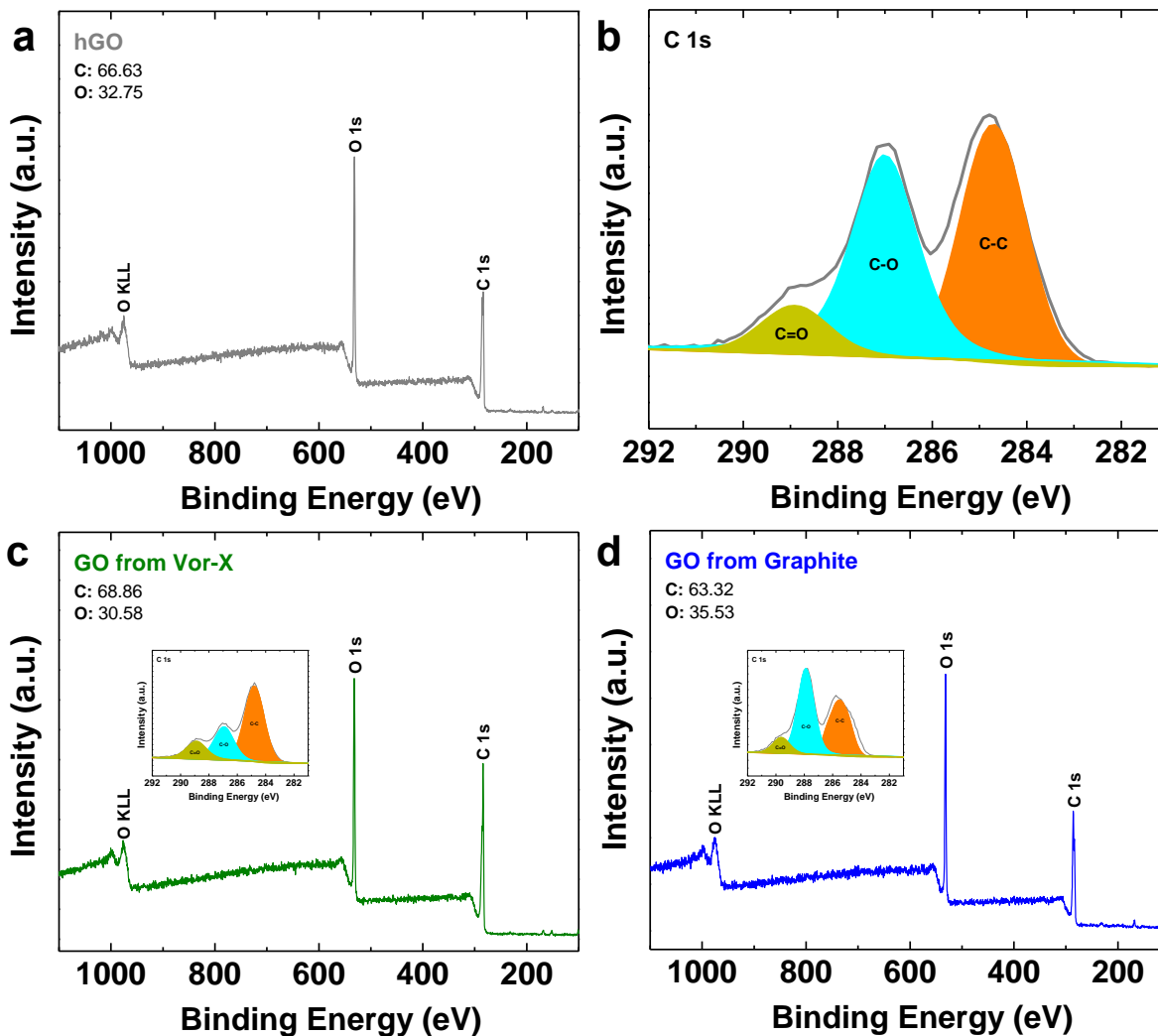


**Figure S12.** Compositional analysis of GO-based powders. XPS spectra of: (a) hGO, (c) GO from Vor-X graphene and (d) GO from natural graphite. Note that (b) and the insets in (c-d) are higher resolution spectra of the C 1s peak of hGO, GO from Vor-X graphene and GO from natural graphite powders, respectively, with corresponding fits to three characteristic peaks:  $sp^2$  and  $sp^3$  C-C at ~284.8 eV (orange), C-O around 287 eV (cyan) and C=O around 289 eV (yellow-green). Based on the atomic percentages of C and O displayed in these plots, the weight percentages for each powder were calculated: hGO powder (59.54% C and 38.98% O), GO from Vor-X graphene (60.95% C and 36.05% O), and GO from natural graphite (55.23% C and 41.29% O).

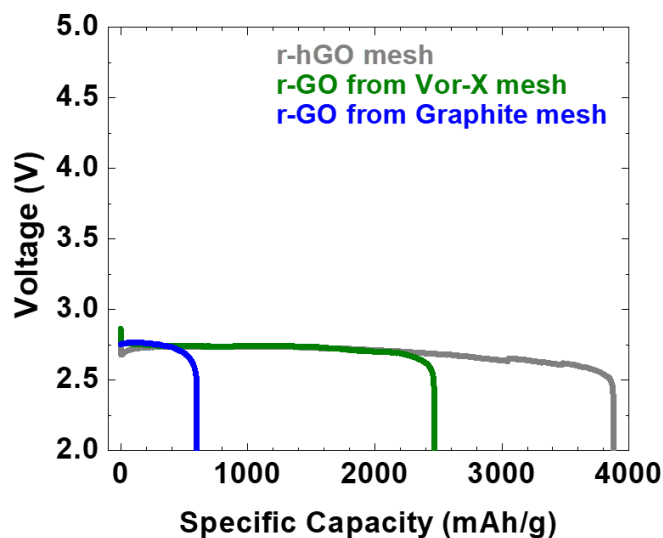


**Figure S13.** Deep discharge (specific capacity) performance of each 3D printed GO-based mesh Li-O<sub>2</sub> cathode at 0.1 mA cm<sup>-2</sup>. The r-hGO mesh outperforms the other 3D printed meshes comprised of non-nanoporous GO-based materials (GO from Vor-X graphene, GO from natural graphite). Note that the specific capacity reported is mAh g<sup>-1</sup><sub>sample</sub> not mAh g<sup>-1</sup><sub>carbon</sub>. The 3D printed GO-based meshes have surface area values approximately 3-6 times higher than the 2D VF films.

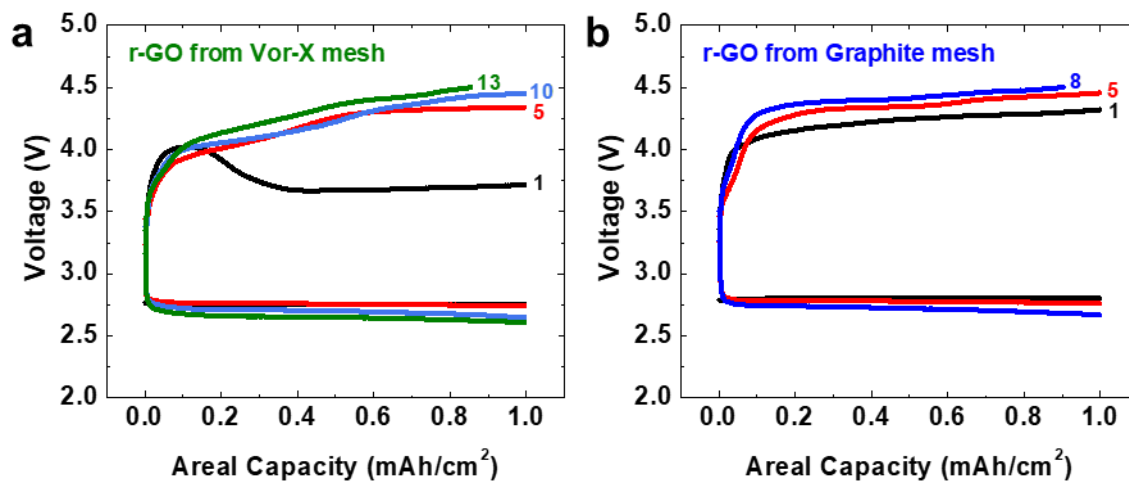


**Figure S14.** Controlled discharge-charge cycling depths (1 mAh cm<sup>-2</sup> at 0.1 mA cm<sup>-2</sup>) of 3D printed GO-based mesh cathodes without nanoporosity: (a) r-GO from Vor-X graphene, (b) r-GO from natural graphite.